A Conceptual Model of an Arctic Sea

P. St-Laurent[1], F. Straneo[2], and D.G. Barber[3]

Abstract. We propose a conceptual model for an Arctic sea that is driven by river runoff, atmospheric fluxes, sea ice melt/growth, and winds. The model domain is divided into two areas, the interior and boundary regions, that are coupled through Ekman and eddy fluxes of buoyancy. The model is applied to Hudson and James Bays (HJB, a large inland basin in northeastern Canada) for the period 1979–2007. Several year-long records from instruments moored within HJB show that the model results are consistent with the real system. The model notably reproduces the seasonal migration of the halocline, the baroclinic boundary current, spatial variability of freshwater content, and the fall maximum in freshwater export. The simulations clarify the important differences in the freshwater balance of the western and eastern sides of HJB. The significant role played by the boundary current in the freshwater budget of the system, and its sensitivity to the wind forcing, are also highlighted by the simulations and new data analyses. We conclude that the model proposed is useful for the interpretation of observed data from Arctic seas and model outputs from more complex coupled/climate models.

1. Introduction

The Arctic seas are characterized by the presence of a sea ice cover, a relatively large river input and positive P (precipitation minus evaporation) rate that contribute to a strong seasonal stratification, and an important control from rotation and topography. A prototype for such seas is HJB (Hudson + James bays), a large inland basin under the influence of a cold Arctic climate [*NSIDC*, 2011; *Maxwell*, 1986]. Like other Arctic basins, HJB is experiencing major changes due to modifications of river runoff [*Déry et al.*, 2005, 2009, 2011], a decreasing ice cover [*Hochheim and Barber*, 2010; *Hochheim et al.*, 2011], and a warming climate [12 of the 19 warmest summers since 1940 have occurred between 1991 and 2009, *Galbraith and Larouche*, 2011]. Understanding and predicting how the marine system responds to these changes is a complex and difficult question. Fortunately, the key drivers of HJB (described in the next section) have been highlighted in the last decades by observations and modeling efforts at the regional scale. A further step would be to synthesize this knowledge into a conceptual model of the system. Such low-complexity models are very useful as an intuitive theoretical background for the interpretation of signals or trends in observations and in complex coupled/climate models [e.g., *Nof*, 2008; *de Verdière*, 2009].

An important application for these conceptual models would be the freshwater (FW) budget of the Arctic Seas. The export of FW from the Arctic can have a strong impact on the global circulation [e.g., *Stouffer et al.*, 2006] but the mechanisms controlling the actual release (or storage) of FW from the Arctic seas remain in many cases obscure. For instance, HJB receives a large fraction [12%, *Lammers et al.*, 2001] of the pan-Arctic river runoff and we do not know which processes control the variability of HJB's FW export to the Labrador Shelf and beyond. The FW budget also determines in many cases the vertical stratification and the exchanges between the euphotic zone and the nutrient-rich deep layers, with direct consequences for biological processes.

In this study we propose a novel conceptual model of an Arctic sea and apply it to the case of HJB. The simple model is driven by a combination of idealized and realistic forcings and it provides a prediction for the evolution of the density field (controlled by salinity/freshwater in Arctic seas) and its circulation. The next section describes the data and modeling studies that support the design of the conceptual model, and a detailed description of the model follows. Then, the model mean state and seasonal cycle are presented and compared with year-long observations from instruments moored at different locations within the basin (the simulated interannual variability will be presented in a separate manuscript). A discussion of the results concludes the study.

2. Results from Previous Studies of HJB

2.1. The Freshwater Budget

The assumptions underlying the conceptual model are motivated by observations and previous studies summarized in this section. Special attention is given to the oceanic freshwater (FW) budget of HJB as it controls the density field of polar seas and the buoyancy-driven component of the circulation. The mean budget comprises the input due to rivers, precipitation and evaporation, lateral exchanges between HJB and the surrounding basins, and the net effect of ice growth and melt at the end of the year. River inflow dominates the budget and amounts to $635\,\mathrm{km^3\,y^{-1}}$ or 12% of the total pan-Arctic runoff [*Lammers et al.*, 2001]. The P rate is poorly constrained by the limited observations, but *Gill* [1982, his Fig. 2.5] suggests a positive value of $290\,\mathrm{kg\,m^{-2}}$ at 60°N ($\approx 220\,\mathrm{km^3\,y^{-1}}$ for HJB), or about three times smaller than the river input. There are very few direct observations of the lateral exchanges between HJB and the neighboring seas (Hudson Strait and Foxe Basin), but estimates can be derived from the literature. Note that the values given are relative to a salinity of 33 psu [the salinity of the bottom layer coming into Hudson Bay, *Prinsenberg*, 1984]. Observations within Hudson Strait show a FW outflow of 23.9–28.0 mSv (750–880 $\mathrm{km^3\,y^{-1}}$) and an inflow whose salinity is

[1]Center for Coastal Physical Oceanography, Old Dominion University, Norfolk, Virginia, USA.

[2]Department of Physical Oceanography, Woods Hole Oceanographic Institution, Woods Hole, Massachusetts, USA.

[3]Centre for Earth Observation Science, University of Manitoba, Winnipeg, Manitoba, Canada.

0148-0227/12/$9.00

too close to the reference value (33 psu) to contribute significantly to the FW budget of HJB [*Straneo and Saucier*, 2008a]. Foxe Basin has a fairly small river input [*Déry et al.*, 2005, 2011] and receives only about $90\,\mathrm{km^3\,y^{-1}}$ of FW from the Arctic [*Straneo and Saucier*, 2008b], so that its influence on the budget of HJB is limited [see *Tan and Strain*, 1996, for a discussion on the intrusion of Foxe Basin waters into HJB]. The volume of FW imported into HJB should hence be relatively small.

The most difficult term to estimate in the mean oceanic FW budget is the net effect of the sea ice cycle. Satellite observations show that the basin seasonally oscillates between a state of completely ice-free waters in August–September, to a fully ice-covered state in January–May [*Hochheim and Barber*, 2010; *Hochheim et al.*, 2011; *Markham*, 1986]. The thickness of the sea ice cover is only known from measurements nearshore [e.g., *Gosselin et al.*, 1990] and qualitative estimates by the Canadian Ice Service (young ice, etc). *Markham* [1986] proposes a mean thickness of 1.6 m for the ice cover. A box budget making use of observations from the Canadian Ice Service suggests that lateral exchanges of sea ice at the mouth of HJB are small [*Murty and Barber*, 1974], which would mean that ice growth and ice melt are approximately balanced for HJB as a whole (small net effect). Note that this does not rule out the existence of redistribution of ice within HJB. Satellite observations show the presence of polynyas in the northwestern part and an eastward drift of ice within the basin [*Barber and Massom*, 2007; *Hochheim and Barber*, 2010; *Hochheim et al.*, 2011], which means that the northwestern area is a net producer of sea ice, and conversely, that the eastern part melts more ice than it produces.

2.2. Hydrography and Circulation

Turning to the hydrography and circulation of HJB, the sea surface salinity shows in both observations and models a nearshore (or boundary) region that gradually freshens as one moves in a counterclockwise (ccw) sense from northwestern HBJ to James Bay, and a saltier interior region (*Prinsenberg* [1986a]; *Lapoussière et al.* [2009]; Fig. 2). The freshening of the boundary is particularly evident at locations where the river discharge is important (Fig. 2). The ccw sense corresponds to the general direction of the surface circulation [*Prinsenberg*, 1986b]. A streamfunction derived from this surface circulation (Fig. 2) highlights the ccw boundary current, and a quiescent interior region having closed streamlines. The vertical structure of the salinity field (that largely controls density in HJB) shows strong stratification around 30 m during the summer [*Prinsenberg*, 1986a] and a wedge of fresh waters surrounding the basin [i.e. the fresh boundary current; *Ingram and Prinsenberg*, 1998].

St-Laurent et al. [2011] conducted realistic simulations with a 3–D, primitive equations, sea ice-ocean coupled model of HJB [see *Saucier et al.*, 2004, for a detailed description of the model]. The 3–D model was spun-up for 20 years using repeatedly the forcings from the period Aug. 2003 to Aug. 2004, until a stationary seasonal cycle was obtained. These forcings included realistic river runoff, high-resolution winds and precipitation from a regional atmospheric model, and tidal and oceanic forcings at open boundaries. The model was used to examine the dynamics behind the cross-shore exchanges of FW between the boundary and interior regions. The cross-shore transport of FW is largely due to Ekman transport, and the seasonality of the wind stress curl yields onshore (offshore) FW transport during the fall (summer) season. These exchanges cause either convergence or divergence of FW within the interior region, which is accurately described by the relation [e.g., *Pedlosky*, 1987, his Eq. 5.12.7]:

$$\boldsymbol{\nabla}\cdot\mathbf{T}_\mathrm{s} = \frac{1}{f\rho_0}\left(\boldsymbol{\nabla}\times\boldsymbol{\tau}_\mathrm{s}\right)_3 \qquad (1)$$

where $\mathbf{T}_\mathrm{s}$ is the Ekman transport in the surface (s) layer, $\boldsymbol{\tau}_\mathrm{s}$ is the wind stress, and subscript 3 denotes the vertical component of the curl. The offshore transport during the summer advects the river waters well beyond the baroclinic Rossby radius (10 km) as can be seen in the observations of *Granskog et al.* [2011, their Fig. 6].

The ice-ocean coupled model also shows that sea ice growth and melt are close to being balanced for HJB as a whole [in agreement with *Murty and Barber*, 1974] so that their net effect over the year is much smaller than the annual river runoff. The simulated precipitation minus evaporation budget is positive and about one third of the river runoff [in agreement with the precipitation-evaporation estimate of *Gill*, 1982] with little seasonality. Finally, the liquid fluxes at the mouth of HJB are dominated by a large outflow in the northeastern part of the basin (25 mSv), the simulated FW export being consistent with observations taken downstream [*Straneo and Saucier*, 2008a]. Very little FW enters the basin through its mouth (2.5 mSv on average, about one tenth of the outflow).

3. Method

3.1. Overview of the Conceptual Model and Main Assumptions

The model configuration is inspired by the work of *Straneo* [2006] and represents an idealized two-layer basin with a cylindrical geometry (r,θ,z), a flat bottom at $z=-H$, and a rigid lid at the surface $z=0$ (see Fig. 3 and Table 1 for definition of the variables). The basin is split into two areas, the boundary and the interior regions. The circulation in the interior is assumed to be weak and negligible, while the boundary region is the host of a two-layer flow (V_1,V_2) whose direction and magnitude are free to evolve over time. The depth of the interface fluctuates in time in both the interior $(D(t))$ and boundary regions $(h_1(\theta,t))$. Exchanges of buoyancy are allowed between the two regions, in the form of surface Ekman transport and eddy fluxes [e.g., *Wåhlin and Johnson*, 2009] in the cross-shore direction. These exchanges allow the interior region to play an active role in the dynamics of the system.

The cross-shore (radial) Ekman transport represents a volume flux between the interior and boundary regions. This flux is assumed to be compensated and canceled by a subsurface flow of opposite direction, so that the vertically-integrated volume flux at $r=R$ is zero at all time and for all θ. This assumption is common in simplified models, the subsurface return flow either taking place in a bottom Ekman layer [e.g., *Newton et al.*, 2006] or as a deep geostrophic flow [e.g., *Pedlosky*, 1987, Chap. 5.12]. The latter option requires a sloping of the interface $\partial D/\partial\theta$ at $r=R$ that is not explicitly simulated in the model since $D(t)$ is the same over the interior region. In fact, $D(t)$ should be viewed as the average position of the interface, i.e. $D(t)=\Theta^{-1}\int\tilde{D}(\theta,t)\,\mathrm{d}\theta$, with the variations due to the longshore slope being in all cases much smaller than the layer thickness.

These simplifications and assumptions are common and appropriate for the basin-wide processes that are of interest in this study. Layered models represent an idealized but physically valid discretization of a real continuous stratification [see *Pedlosky*, 1987, Chap. 6.18 for a discussion]. The rigid lid expresses the fact that adjustments of the free surface are nearly instantaneous at the timescales of interest (daily and longer), and that deviations from an undisturbed sea surface are negligible compared to the layer thickness. The assumption of a flat bottom prevents any topographic steering, but this steering is recovered in the model by assuming a strong boundary current that flows along the

shorelines of the basin, and a quieter interior region. There is no lateral friction in the model (free-slip). The dynamics are geostrophic with the exception of Ekman and eddy fluxes whose effects on the large scales are parameterized (see the next section). The latitudinal variations of the Coriolis parameter are also neglected given the modest size of the basin (f-plane). The next sections describe in further details the model equations.

3.2. Model Equations

We first define an equation of state in salinity S (appropriate for polar regions), a FW concentration c, and FW thickness $h_{\rm fw}$:

$$\rho \equiv \rho_0(1+\beta S), \qquad c \equiv \frac{S_2-S_1}{S_2} = \frac{\rho_2-\rho_1}{\rho_2-\rho_0}, \qquad h_{\rm fw}(\theta,t) \equiv c\,h_1(\theta,t), \tag{2}$$

where β, ρ_0 and ρ_2 are constants given in Table 1, and $c=1$ ($c=0$) is pure (absence of) FW. Note that the density ρ_1, ρ_2 (or salinity S_1, S_2) of the two layers is fixed in time and space so that the volume of FW within the water column is totally determined by the thickness of the upper layer (FW is absent from the deeper layer). Density ρ_1 is a constant obtained by solving the model equations in steady state with time-averaged forcings (see Appendix A).

The velocities in the boundary region, $V_1(\theta,t), V_2(\theta,t)$, are obtained from the thermal wind relation $\partial v/\partial z = -g(f\,\rho_0)^{-1}\,\partial\rho/\partial r$ and from the wind stress curl forcing:

$$V_1 - V_2 = -\frac{2g'}{f\,L}\left(H - h_1 - D\right), \tag{3}$$

$$T_{\rm riv}(\theta,t) \simeq -\frac{1}{R+L}\frac{\partial}{\partial\theta} L\,T_\theta, \quad T_\theta(\theta,t) \equiv V_1\,h_1 + V_2\,h_2, \tag{4}$$

$$T_\theta^{\rm ups}(t) \equiv a\,H\,\overline{\zeta}(t), \tag{5}$$

where $g' \equiv g\,(\rho_2-\rho_1)/\rho_0$, T represents vertically-integrated velocities ('transport', in $\mathrm{m^2\,s^{-1}}$), $T_{\rm riv} \le 0$ is the radial transport at $r = R+L$ due to river discharge, and T_θ is the transport due to the boundary current. The value of T_θ is prescribed at the upstream side of the boundary current as a linear function of the wind stress curl forcing $\overline{\zeta}$ (see Section 3.3). The overline denotes an average over the area of the interior region:

$$\overline{\zeta} = \frac{1}{A}\int_{R_0}^{R}\int_0^{\Theta} \zeta\, r\,{\rm d}\theta\,{\rm d}r, \tag{6}$$

The thickness of the layers is obtained by vertically integrating (from bottom to surface) the advection-diffusion equation $\partial c/\partial t = -\boldsymbol{\nabla}\cdot c\mathbf{v} + \boldsymbol{\nabla}\cdot\overline{\mathbf{v}'c'}$ and making use of the divergence theorem:

$$\frac{{\rm d}D}{{\rm d}t} = \frac{\overline{\zeta}}{\rho_0 f} - \frac{P+M}{c} - \frac{2v^*}{A}\int_0^{\Theta}(h_1-H+D)^2\,\frac{R}{L}\,{\rm d}\theta, \tag{7}$$

$$\frac{\partial h_1}{\partial t} = -\frac{\delta\theta}{\delta B}\frac{\partial}{\partial\theta}LV_1h_1 + \frac{A\overline{\zeta}}{\rho_0\,f\,\delta B}\frac{\delta\theta}{\Theta} - \frac{T_{\rm riv}(R+L)\delta\theta}{c\,\delta B} + \frac{P+M}{c} - \frac{2v^*R\,\delta\theta}{L\,\delta B}\left(h_1-H+D\right)^2, \tag{8}$$

$$h_1(\theta=0) = \frac{\rm FWI}{L\,V_1\,c}. \tag{9}$$

Equation 7 (Eq. 8) is valid in the interior (boundary) region. The terms involving $\overline{\zeta}$ (v^*) represent the exchange of FW between the interior and boundary that is due to surface Ekman transport (eddies). The terms with P (precipitation minus evaporation rate, in $\mathrm{m\,s^{-1}}$) and M (sea ice melt minus growth rate, in $\mathrm{m\,s^{-1}}$) are the surface buoyancy fluxes (prescribed as a forcing). The two remaining terms are the contribution from FW advection by the boundary current, $\partial/\partial\theta\,(L\,V_1\,h_1)$, and the river discharge, $T_{\rm riv}$. The function $\delta B(\theta) = 0.5\,\delta\theta\left[(R+L)^2 - R^2\right]$ is the area of a slice $\delta\theta$ of the boundary region. FWI is the FW inflow prescribed at the upstream boundary (Table 1).

The terms that correspond to Ekman and eddy fluxes of FW deserve further explanations. The cross-shore flux of FW due to Ekman transport ($\mathbf{T}_{\rm s}$) is derived from $\mathbf{T}_{\rm s} = -\mathbf{k}\times\boldsymbol{\tau}_{\rm w}\,(f\rho_0)^{-1}$ and the divergence theorem:

$$\frac{1}{A}\int_{R_0}^{R}\int_0^{\Theta}\boldsymbol{\nabla}\cdot\mathbf{T}_{\rm s}\,r\,{\rm d}\theta\,{\rm d}r = \frac{\overline{\zeta}}{\rho_0 f}, \tag{10}$$

where $\boldsymbol{\tau}_{\rm w}$ is the wind stress. Following *Spall* [2004] and *Straneo* [2006], the eddy flux is parameterized as the product of the property contrast δc between interior and boundary regions and the slope of the interface in the radial direction, with an adjustable coefficient v^* (discussed in section 8):

$$\overline{\mathbf{v}'c'}(z,\theta,t) = \begin{cases} v^*c\,\frac{h_1-H+D}{L/2} & \text{if } H-D<z<h_1, \\ 0 & \text{elsewhere } (\delta c=0). \end{cases} \tag{11}$$

The next sections describes the parameters of the model, the boundary conditions, and the forcings used for prognostic simulations of HJB.

3.3. Boundary Conditions for the Boundary Current

The transport value upstream of the boundary current, $T_\theta^{\rm ups}(t)$, is prescribed as a function of the wind stress curl (Eq. 5). Previous numerical experiments [*Wang et al.*, 1994] support this view that the vertically-integrated circulation of HJB is mostly wind-driven (at least during the summer period). We provide in Fig. 4 and Table 2 new data analyses that further support Eq. 5. The figure shows that velocities from two different locations follow the seasonality of the wind stress curl [taken from *Mesinger et al.*, 2006] averaged over the interior region of HJB. The timeseries were lowpass filtered on a common timescale (40 days), linearly detrended, adjusted for a potential lag, and divided by their standard deviation. Note the high coherence between velocities at different depths. The water depth is approximately 110 m at station A and 130 m at station B.

Correlation and regression between the velocity data and the curl are given in Table 2. Significant correlations are obtained for all the timeseries ($R\sim0.65$, $p\le0.01$) except the near-surface velocity at station A ($R=0.35$, $p=0.18$). Fig. 4 shows that this is mostly related to a specific wind event in May 2004 that is not observed in the velocity data. The table also shows that currents have little or no shear at station A, while at station B velocities vary by as much as $5\,\mathrm{cm\,s^{-1}}$ between 28 m and 58 m. Finally, it is seen that the coefficient of proportionality between curl and velocities is roughly similar between stations and depths. These results derived from the velocity data are exploited in the model by parameterizing the transport within the boundary current as in Eq. 5 where the coefficient of proportionality corresponds to an average of the values in Table 2. A theoretical justification for the parameterization is given in Appendix B.

The wind stress curl sometimes changes in sign and the flow direction changes accordingly (Eq. 5). When this happens, the transport $T_\theta^{\rm ups} < 0$ is prescribed at $\theta=\Theta$ instead of $\theta=0$, and its value is again extrapolated for $0\le\theta\le\Theta$

using Eq. 4 and by assuming the river discharge always follows the direction of the wind-driven current. The value $h_1(\theta = \Theta, t)$ is a priori unknown during such events and thus we assume the usual no-gradient condition, i.e. $h_1(\theta = \Theta, t)$ is taken from the closest interior grid point. Once the situation goes back to normal, $h_1(\theta = 0, t)$ is gradually relaxed to the value required for a constant FW inflow (Eq. 9). In all cases the layer velocites V_1, V_2 are calculated from Eq. 3.

3.4. Model Parameters and Forcings

The geometry of the model (parameters f, Θ, H, R, L, A, B; see Table 1) is obtained from the Etopo database [*NOAA*, 2006] and from the numerical experiments of *St-Laurent et al.* [2011]. The radius $R + L$ is chosen so that $\Theta(R + L)$ represents the perimeter of the basin (about 3500 km). The interior region of the conceptual model is defined as the area within $R_0 < r < R$ and $0 < \theta < \Theta$ (Fig. 3), with R_0 chosen as to preserve the area A estimated by *St-Laurent et al.* [2011, their Fig. 4]. Note that the exact shape of the interior region is unimportant since its properties are assumed to be horizontally homogeneous. The width L of the boundary current is assumed constant for simplicity.

The surface forcings have P and M uniform in space and P uniform in time. A constant P is reasonable given the relatively small role it plays in the FW budget [*St-Laurent et al.*, 2011, their Table 1]. The sea ice melt (growth), $M(t)$ in $\mathrm{m\,s^{-1}}$, is represented as a sinusoid over an interval $0, \pi$ $(\pi, 2\pi)$ that corresponds to 1 May to 1 August (1 December to 1 May). The amplitude of the sinusoid is fitted so that ice thickness seasonally oscillates in the range 0–1.47 m (see Fig. 5). This range leads to a volume of ice similar to that of *St-Laurent et al.* [2011, their Table 1]. A salinity of $S_{\mathrm{ice}} = 5$ psu and a density $\rho_{\mathrm{ice}} = 900\,\mathrm{kg\,m^{-3}}$ are assumed (see Table 1). The effect of spatial variations in M are examined in Section 6.

The river forcing has two components, a seasonal (monthly) climatology, and a normalized scaling factor. The monthly climatology is taken from *Saucier et al.* [2004, see its description therein], and it features 53 different river outlets located around HJB that deliver 20.2 mSv of FW on average. Each river outlet is placed at a position $\theta\,(R + L)$ that reflects its true location along the perimeter of the basin. The monthly climatology is interpolated in time to yield a smooth forcing (Fig. 5).

The seasonal river climatology $T_{\mathrm{riv}}^{\mathrm{clim}}(\theta, t)$ is supplemented by the normalized scaling factor $\psi(t)$, whose role is to add an interannual modulation that applies to all rivers at the same time:

$$T_{\mathrm{riv}}(\theta, t) = T_{\mathrm{riv}}^{\mathrm{clim}}(\theta, t)\ \psi(t) \tag{12}$$

The factor $\psi(t)$ corresponds to the ratio between the total discharge of a given year and the mean value of the total discharge. It is estimated using all the HJB river timeseries available in the International Polar Year Arctic Freshwater Systems database [*Déry et al.*, 2009, http://nhg.unbc.ca/ipy/index.html], and it fluctuates between $\psi = 0.82$ (minimum, year 1989) and $\psi = 1.25$ (maximum, 2005; see Auxiliary material).

Winds are taken from the high-resolution (30 km, 3-hourly) North American Regional Reanalysis [NARR, *Mesinger et al.*, 2006]. Wind stress curl $\zeta\,(x, y, t)$ is calculated at each grid point and then averaged over the interior domain of HJB [as defined in *St-Laurent et al.*, 2011] to yield $\overline{\zeta}(t)$ (see Auxiliary material). A daily climatology built from this dataset over the period 1979–2007 is shown in Fig. 5. Curl values are lowest in the summer and highest during the fall, with frequent shifts in sign (negative values occur over 50 days in the daily climatology of Fig. 5).

3.5. Simulations Performed

We present in the study the results from two prognostic simulations: 1) a control simulation that makes use of the forcings described in the previous section, and 2) a simulation identical to 1) except for sea ice growth/melt that is non-uniformly distributed over the domain (see section 6). Both prognostic simulations are run over the full 1979–2007 period of the forcings without halt or restoring conditions (see Auxiliary material). The initial condition used for the two prognostic simulations is the solution of Eqs. 4,7,8 with time derivatives set to zero and with forcings averaged over the full 1979–2007 period. In other words, the initial condition of the prognostic simulations is the solution to the steady problem.

3.6. Observations

Year-long observations were obtained from three moorings (Stations A, B, C) in key locations of HJB (Fig. 1). Technical information about the instruments used, the sampling frequency, and the quality control applied, are available from the following sources: *Straneo and Saucier* [2008a] for Station C, and the Canadian Department of Fisheries and Oceans at http://slgo.ca/app-sgdo/en/accueil.html (Stations A,B). Note that the instrument records include high-frequency variability (tidal and inertial oscillations) that are absent from the simulated variables. To ease the comparison and to highlight the low-frequency seasonality, the timeseries are low-pass filtered on a common timescale (40 days).

4. The Simulated Mean State

An overview of the mean state simulated by the model over the period 1979–2007 is shown in Fig. 6. The FW thickness (or FW content) is 1–3 m during the winter and 4–5 m during the summer, with a seasonal range of 2.4 m on average. This range is close to those reported by *Prinsenberg* [1988, 2.7 m in southeastern HJB, and 3.0 m in western HJB]. The summer values of 4–5 m and the general increase from upstream to downstream are also consistent with observations from the ice-free period [e.g., *Prinsenberg*, 1984, his Fig. 1]. The increase is particularly large around 100, 900, and 2200 km, these locations corresponding to those of the three main river discharges (Thelon River, Nelson River, and James Bay; see map on Fig. 1). An approximate expression for $h_1(\theta)$ in steady state is:

$$h_1(\theta) \approx h_1^0 + \frac{\frac{A\,\overline{\zeta}}{\rho_0\,f\,\Theta}\theta - \frac{1}{c}\int_0^\theta T_{\mathrm{riv}}(R+L)\,\mathrm{d}\theta' + \frac{P+M}{c}\frac{\delta B}{\delta\theta}\theta}{L\,V_1^0 + h_1^0\,2g'\,(H - h_1^0)\,/(f\,H)} \tag{13}$$

where $h_1^0 \equiv h_1(\theta = 0)$ and $V_1^0 \equiv V_1(\theta = 0)$. The denominator represents an average velocity for the boundary current. The numerator is the sum of all FW inputs in the boundary area (onshore Ekman transport, rivers, precipitation and ice melt). Eq. 13 clearly shows how the river runoff T_{riv} is collected by the boundary current and thus contributes to the deepening of the pycnocline as θ increases.

Waters enter HJB in both the upper and lower layers at the upstream boundary of the model (northwestern HJB) before velocities become increasingly sheared going downstream (Fig. 6). This is a consequence of the thickening of h_1 that increases the cross-shore density gradient (thermal wind, Eq. 3). The upper layer thus speeds up downstream while the lower layer slows down in response to the freshwater inputs (mostly rivers). V_2 is slightly negative at the downstream boundary ($-3\,\mathrm{cm\,s^{-1}}$) as in the observations that will be presented later (section 7). The velocity in the upper layer varies from $2\,\mathrm{cm\,s^{-1}}$ upstream to $10\,\mathrm{cm\,s^{-1}}$ downstream.

The thickening of the fresh layer and the increase of the surface velocity from upstream to downstream require an upward diapycnal velocity Ω that balances the horizontal divergence within the boundary current:

$$\Omega = -\frac{1}{\delta B}\frac{\partial}{\partial\theta} L\, V_2\, h_2. \tag{14}$$

The upward flow is concentrated at the location of the rivers and its seasonality closely follows the local river runoff (maximum at freshet, i.e. the period when snow melts and the river discharge peaks). The mean diapycnal velocity integrated over the whole boundary region is an upward flux of 0.24 Sv that balances the horizontal inflow upstream (0.03 and 0.11 Sv in upper and lower layers), rivers (0.02 Sv), and the transports downstream (0.29 Sv and −0.13 Sv in upper and lower layers; see Fig. 7). Thus the buoyancy inputs (notably rivers) transform what was essentially a salty inflow on the northwestern side ($h_2\, V_2 \gg h_1\, V_1$) into a brackish outflow on the northeastern side ($h_1\, V_1 \gg h_2\, V_2$; see Fig. 6). The salt budget of the system is discussed in Appendix C.

The Ekman transport between the interior and boundary regions leads to an additional vertical circulation. The mean wind stress curl is cyclonic and produces onshore (offshore) surface (bottom) transport, and downwelling (upwelling) in the boundary (interior) regions. The magnitude of this overturning cell is given by Eq. 10, and its mean value is about −0.06 Sv (negative for downwelling). This is much smaller than the upwelling caused by the buoyancy-driven circulation, and so the vertical flow within the boundary current remains upward.

5. The Simulated Seasonal Cycle

We now move on from the mean state to seasonal timescales and examine how the system balances the sources and sinks of FW over the year. Figure 8 shows all the terms from the FW budget (Eqs. 7,8) in the boundary and interior regions. The two areas have different seasonal evolutions since the interior is isolated except for Ekman and eddy fluxes. As a consequence, ice growth in the interior is essentially balanced by ice melt, with secondary contributions from Ekman transport (a sink) that counteracts eddy fluxes and positive P (sources).

The boundary region shows a more complex balance. We first notice that both ice melt and river freshet attain their peak in early summer which results in a large and rapid freshening (+2 m within 2 months). The FW content remains high over the next five months (August to January) even though several processes are active in the background. Of these processes, rivers and onshore Ekman transport are responsible for bringing large amounts of FW to the boundary, O(10 cm week^{-1}). These inputs are, however, largely compensated by the cyclonic circulation that collects and removes that FW. The FW export remains high until January when the river runoff and Ekman transport have become much smaller. Meanwhile the ice growth gradually removes the FW that remains in the water column until a minimum is reached in May (maximum ice cover), completing the seasonal cycle.

The FW export (FWE) thus plays a significant role and its seasonality is best understood by rewriting Eqs. 3,4 as:

$$\begin{aligned}\mathrm{FWE}(t) &\equiv (V_1\, h_1\, L\, c)\,(\theta=\Theta,t) \\ &= \left[\frac{T_\theta}{H} + \frac{2g'}{f\, L\, H}\,(H-h_1)\,(h_1 - H + D)\right] h_1\, L\, c\end{aligned} \tag{15}$$

The first term, T_θ/H, is the velocity of the upper layer in the absence of density gradients $\partial\rho/\partial r$ (i.e. the barotropic velocity), and should be interpreted as the Contribution of Winds (CW) to the FWE. The second term is a correction for $\partial\rho/\partial r \neq 0$ that tends to accelerate the upper layer; it is the Contribution of Buoyancy inputs (CB) to the FWE. The relative importance of these two contributions in the seasonal FWE is calculated as:

$$\begin{aligned} CW(t) &\equiv \langle CW\rangle + CW'(t), \qquad CB(t) \equiv \langle CB\rangle + CB'(t), \\ \mathrm{FWE}(t) &= \langle CW + CB\rangle \\ &\quad \left(1 + \frac{CW'}{\langle CW+CB\rangle} + \frac{CB'}{\langle CW+CB\rangle}\right)\end{aligned} \tag{16}$$

where $\langle . \rangle$ is an annual mean and the primes denote the seasonal variability (plotted in Fig. 9). The contribution of buoyancy, CB', essentially follows the variations of $h_1(\theta=\Theta,t)$: highest in January and lowest around May (it will be shown later that this seasonality is consistent with the local salinity, Fig. 13). The contribution from winds is most important during the fall when it enhances the FWE by 30%. It is worthwhile to note that CB' and CW' lead to a seasonality radically different from that of the river freshet and ice melt (both maximum around June, see Fig. 8). The lag between CB' and the river freshet is simply the time required for the river waters to reach the downstream end of the domain.

Going back to the seasonal budget (Fig. 8), we see that the processes coupling the interior to the boundary play a small but significant role in the budget. The most obvious contribution is onshore Ekman transport during the fall season with a magnitude about half of the river input. Offshore Ekman transport occurs as short events (∼ one month) randomly distributed between March and September so that their contribution is very small in the climatology shown in Fig. 8. These events are accompanied by a reversal of the boundary current and a sudden salification of the boundary region, as can be seen in the observations and model results for April 1993 (Figs. 11,13). Eddies also represent a small but constant flux of FW from the boundary to the interior. The fluxes never reverse since the boundary is always fresher. The mean contribution from eddy fluxes is comparable to the net evapotranspiration rate and represents about 30% of the mean Ekman transport.

6. Ice Growth in Polynyas

We complement the spatially-averaged results from the previous section by presenting the seasonal FW balance for two specific locations representative of the western and eastern parts of the domain, respectively. To further highlight the spatial differences, the results are taken from Run #2 (see section 3.5) where ice growth (melt) is increased by 30% in the western (eastern) part to mimic the presence of HJB's latent-heat polynya. The melt function $M(t)$ is thus modified as:

$$M'(\theta,t) = M(t)\left[1 - \Gamma\cos\left(\frac{\theta\,\pi}{\Theta}\right)\,\mathrm{sgn}\{M(t)\}\right] \tag{17}$$

where $\Gamma \geq 0$ is an adjustable parameter set to 0.3. Note that the total ice growth/melt is preserved, and the rates in the interior region are left unmodified. The FW balance at the two locations is shown in Fig. 10.

We first note that the FW thickness in the two locations differ by as much as 2.5 m since one is located upstream of the main rivers and the other one is downstream. Note also that the FW content in western HJB falls down to 1 m in April. This area is therefore likely to produce waters with salinities greater than $S_2 = 33$ psu during the winter. In fact, the whole western side entirely relies upon the rivers upstream (Thelon River, see Fig. 1) and Ekman transport

(that brings FW during the fall season) to compensate for the unbalanced ice cycle that has a 30% excess growth. The freshet occurs relatively late in this area (July) and the river waters are rapidly advected away by the cyclonic circulation in September and October. These conditions favor the low FW content that characterizes this area.

On the eastern side of the bay, the excess melt is seen to produce a very rapid increase in FW thickness during the summer season. This area is also over the trajectory of all the rivers pulses from upstream so that the local FW content remains high all over the fall period. For instance, the advective term has a peak in June (November) associated with the river pulse coming from James Bay (Thelon and Nelson rivers). It is only once winter begins and the river flow upstream has decreased that advection becomes a sink of FW. Another contrast with the western location is that the eddy fluxes here play a significant role all over the year. This is expected since the FW gradient between the interior and boundary is larger here. Furthermore, velocities are higher in this part of the domain (Fig. 6) and it favors the baroclinic instabilities parameterized by Eq. 11. So even though the net annual change in FW is zero at both locations, it is clear from these results that the relative importance of the different forcings and processes vary considerably between these two areas.

7. Comparisons with Observations

The results of the model are now compared to the observations available. Fig. 11 shows the velocities at two different depths at the downstream boundary of the model (station B, see Fig. 1). Simulated and observed values are close one to another although the model slightly underestimates the variability (in part because of the use of a constant value for the coefficient a in Eq. 5). The mean model velocity is also slightly higher than observed owing to the fact that the flow is sheared (see v_0 in Table 2) and that observed and modeled depths differ (28 m and 15 m, respectively). The shear is visible in both model and data when one compares the upper and lower velocities. Extrapolating the observed velocity profile to model depth (15 m) increases the observed values by $\sim 3\,\mathrm{cm\,s^{-1}}$, i.e. closer to model results. Note that the velocities in the deeper layer are mostly negative so that deep water enters HJB at this location.

Fig. 12 shows a similar comparison at the upstream boundary (station A, see Fig. 1). In contrast with the previous location, velocities here are slow (few $\mathrm{cm\,s^{-1}}$) and exhibit very little shear and variability. Therefore the boundary current evolves from a barotropic flow upstream (station A) to a strongly baroclinic flow downstream (station B). We note that the model reproduces this important transition very well.

Salinity data are available for Station B at a depth of 28 m or approximately the depth of the model interface. Salinity and FW are related (Eq. 2) and one can be used to estimate the other. In the model, S_1 and S_2 are fixed and h_1 varies in time. Another possibility would be to consider h_1 as constant (i.e. equal to its mean value $\langle h_1 \rangle$) and to have S_1 that varies in time:

$$h_{\mathrm{fw}}(t) = \frac{S_2 - S_1}{S_2} h_1(t) \Leftrightarrow \frac{S_2 - S_{\mathrm{pseudo}}(t)}{S_2} \langle h_1 \rangle \qquad (18)$$

We use this equivalence to define the model pseudo-salinity and compare it to the record from Station B in Fig. 13. The data shows freshening from summer to fall, and salification during winter and spring. The model salinity agrees very well with the data in both timing and amplitude.

Another quantity that constrains the seasonality of FW is its flux downstream of the basin. Fig. 14 shows the comparison between observations from Station C [*Straneo and Saucier*, 2008a] and modeled flux at Station B (i.e. at the downstream boundary of the model). Both observed and simulated curves illustrate a large outflow during the fall season, and minimal flux during spring. The mean simulated flux over this period is 33.0 mSv and 29.5 mSv on average over 1979–2007. This suggests that the FW outflow was relatively large in that particular year. The mean flux from the data is not as large however (27.1–28.0 mSv). This is likely related to the use of a perfectly balanced sea ice cycle in the model. More realistic simulations suggest that ice growth exceeds the melt by about $80\,\mathrm{km^3\,y^{-1}}$ [*St-Laurent et al.*, 2011], which represents a sink of 2.5 mSv not taken into account here. Nevertheless, we conclude from these comparisons with the data that the model reproduces reasonably well the key features defining the seasonal cycle of HJB (see also Table 3 for a quantitative comparison between observed and simulated quantities).

8. Sensitivity of the Results

The model depends on parameters and forcings (Table 1) that are for the most part constrained by observations. Two exceptions to this are the eddy flux efficiency v^* and the sea ice cover. The sensitivity of the results to the latter has been examined by varying the maximum thickness of ice and the spatial distribution of ice growth and melt. We find that the qualitative features of the solutions are the same in all the experiments. The main impact of varying the ice thickness is an amplification/damping of the seasonal ice growth/melt pattern of Fig. 8 without much effect on the other components of the budget. Similarly, increasing ice growth (melt) in the western (eastern) part of the basin simply enhances features that are already present in the control simulation (e.g., the low FW content on the western side of HJB during wintertime).

The eddy fluxes parameter v^* was also varied between 0 and $5\,\mathrm{m\,s^{-1}}$. We observe that increasing this parameter leads to more FW being transferred to the interior and thus a freshening of this region (ρ_1 decreases, c increases). A more formal way to understand this result is to acknowledge that c is obtained by solving Eq. 7 with $\partial/\partial t \to 0$. A larger v^* value within this equation simply requires a larger c value. The effect on c is small however: increasing v^* from nothing to $5\,\mathrm{m\,s^{-1}}$ only doubles c ($0.07 \leq c \leq 0.15$ and $1022.4 \leq \rho_1 \leq 1024.6\,\mathrm{kg\,m^{-3}}$ for $0 \leq v^* \leq 5\,\mathrm{m\,s^{-1}}$). We also note that the resultant of Ekman and eddy fluxes must be directed onshore, irrespective of v^*. This is again a constraint from Eq. 7 that requires, in steady state, a fixed onshore flux of FW to balance its positive precipitation minus evaporation budget. The eddies cannot provide such an onshore flux (diffusion must be downgradient, i.e. directed offshore). Therefore, Ekman transport necessarily dominates the cross-shore exchanges of FW and the results are qualitatively the same for all values of v^*.

9. Discussion

The comparison with observations suggests that the simple model proposed here successfully captures the large-scale features of the system. It seems however difficult to introduce further simplifications to the model as it would significantly impact the results. For instance, a horizontally-averaged model would lack the large divergence introduced by the boundary current, and also the important differences between the freshwater balance in western and eastern parts of the domain. Similarly, a depth-averaged model would miss the strong baroclinity of the boundary current and its acceleration as it moves downstream. Nevertheless, the relative simplicity of Eqs. 4,7,8 suggests that the model could

be amenable to complete analytical solutions if additional assumptions were introduced. Such solutions have the advantage of revealing explicitly the physics of the system (e.g., Eq. 15).

One of the key model assumptions is the simple linear relationship between transport and wind stress curl (Eq. 5; Appendix B). We could expect a more complicated equation involving e.g. the influence of the ice cover on ocean dynamics. The simulations of *St-Laurent et al.* [2011, their Fig. 5d] suggest that sea ice filters about 50% of the wind stress curl in May (maximum ice thickness). We tried to include such ice insulation effect in the conceptual model by reducing $\overline{\zeta}$ by various amounts during the winter. The best model-data comparison is, however, obtained with no damping of $\overline{\zeta}$. Additional data and experiments with realistic models would be required to properly parameterize the effect of winter sea ice on the transfer of momentum.

The simple model also offers some insight into the effects of climate change in HJB. Changes in wind patterns or intensity [*Wan et al.*, 2010] would have a direct impact on the velocity of the boundary current, and in turn, on the FW export from the basin (Eq. 15). More cyclonic (anticyclonic) winds would favor a larger export (storage) of FW and a saltier (fresher) basin. Similar changes may take place in other Arctic seas and the model proposed here seems a relevant tool for their study.

10. Conclusions

We proposed a conceptual model of an Arctic sea driven by winds, rivers, atmospheric fluxes, and sea ice. The model was applied to Hudson and James Bays and the results are consistent with several year-long records from moored instruments. The model reproduces the seasonal migration of the halocline, the baroclinic boundary current, the spatial variability of freshwater content, and the fall maximum in freshwater export. The simulations show that freshwater inputs and sinks are balanced in very different ways in different regions of HJB (the ice growth dominated western area versus the ice melt dominated eastern area). Both the model and new data analyses further show that the boundary current is sensitive to the curl of the winds above the basin. The model proposed is useful for the interpretation of observed data from Arctic seas and model outputs from more complex coupled/climate models.

Appendix A: Numerical Solution of the Model Equations

The solution procedure includes two stages. First, the model equations (4,7,8) are solved in steady state ($\partial/\partial t \rightarrow 0$) with time-averaged forcings. Then, this steady solution is used as the initial condition for the prognostic (time-evolving) simulation. The steps for the solution of the steady state are:

1. Get boundary current transport $T_\theta(\theta)$ from Eqs. 4,5.

2. Get $V_1(\theta = 0)$ by assuming a barotropic inflow at $\theta = 0$ (see observations, Fig. 12):

$$V_1(\theta = 0) = T_\theta(\theta = 0)/H \tag{A1}$$

3. Solve the coupled Eqs. 7,8 iteratively. For the first iteration we assume that $v^* = 0$:

(i) Get c from Eq. 7.

(ii) Get $h_1(\theta = 0)$ from Eq. 9.

(iii) Get $D = H - h_1(\theta = 0)$ (from Eq. 3 and barotropic inflow assumption).

(iv) Get $V_1\, h_1(\theta)$ by integrating Eq. 8 in θ.

(v) Get $h_1(\theta)$ by combining Eqs. 3,4 and solving the cubic equation that results:

$$h_1^3 + (D - 2H)\, h_1^2 + \left[-\frac{L\, T_\theta\, f}{2g'} + H(H - D) \right] h_1 = -\frac{f\, L\, H}{2g'} V_1 h_1 \tag{A2}$$

4. The subsequent iterations are similar except that $v^* \neq 0$. The iterative procedure goes on until h_1 and c converge. ρ_1 is then obtained from c through Eq. 2.

5. Get $V_1(\theta)$ from $(V_1 h_1)(\theta)$ and $h_1(\theta)$. Get $h_2(\theta)$ from $H = h_1(\theta) + h_2(\theta)$.

6. Get $V_2(\theta)$ from Eq. 4.

A timestep of the prognostic calculation follows these steps:

1. Update wind and river forcings: $\overline{\zeta}(t), T_{\rm riv}(\theta, t)$.
2. Update $T_\theta(\theta, t)$ from Eqs. 4,5.
3. Update $h_1(\theta = 0, t)$ from Eq. 9.
4. Update $D(t)$ (Eq. 7) and $h_1(\theta, t)$ (Eq. 8).
5. Update $V_1(\theta, t)$ by combining Eqs. 3,4 into:

$$V_1 = \frac{T_\theta}{H} - 2g' \frac{H - h_1}{H} \frac{H - h_1 - D}{f\, L} \tag{A3}$$

6. Variables $h_2(\theta, t)$ and $V_2(\theta, t)$ follow directly from $H = h_1 + h_2$ and Eqs. 3,4.

The update of D and h_1 is performed with a two-stage predictor-corrector algorithm (Heun's method).

Appendix B: On Transport, Winds, and Rivers

The velocity data (Fig. 4, Table 4) show a linear relationship with the wind stress curl averaged over the interior region of HJB. Such relationship is interpreted by examining the steady, depth-averaged momentum equation. Assuming an f-plane, rigid lid and flat bottom, small Rossby and horizontal Ekman numbers, and a linear bottom friction of the form $\boldsymbol{\tau}_{\rm b} \equiv \rho_0 \epsilon \mathbf{T}$, the application of the curl operator $\boldsymbol{\nabla}\times$ on the momentum equation yields a simple balance between wind stress curl and bottom stress curl (see section 3.1 for a discussion of these assumptions):

$$\begin{aligned} (\boldsymbol{\nabla} \times \boldsymbol{\tau}_{\rm w})_3 &= (\boldsymbol{\nabla} \times \boldsymbol{\tau}_{\rm b})_3\,, \\ \zeta &= \rho_0\, \epsilon\, (\boldsymbol{\nabla} \times \mathbf{T})_3 \end{aligned} \tag{B1}$$

where the subscript 3 denotes the vertical component, and $\mathbf{T}(r, \theta, t)$ (in m^2 s^{-1}) is the transport (depth-integrated velocity) within the basin. Then, averaging the left and right hand sides over the interior region of the basin leads to:

$$\overline{\zeta} = \frac{\rho_0\, \epsilon}{A} \int_{R_0}^{R} \int_{0}^{\Theta} \frac{1}{r} \left(\frac{\partial}{\partial r} r\, T_\theta - \frac{\partial T_r}{\partial \theta} \right) r\, {\rm d}\theta\, {\rm d}r$$

$$\Rightarrow \qquad T_\theta(r = R, t) \approx \frac{A\, \overline{\zeta}}{\rho_0\, \epsilon\, \Theta\, R}, \tag{B2}$$

where the transport in the radial direction, T_r, was assumed negligible compared to T_θ. Eq. B1 is a theoretical prediction for the transport within the boundary current. The value of the friction coefficient ϵ can be derived from the usual quadratic bottom friction:

$$\epsilon \equiv \frac{|\boldsymbol{\tau}_{\rm b}|}{\rho_0 T_\theta} \sim \frac{\rho_0 C_{\rm D} V_\theta^2}{\rho_0 T_\theta} = \frac{C_{\rm D} V_\theta}{H} \tag{B3}$$

Using typical values $C_D = 2.5 \times 10^{-3}$, $V \sim 0.05\,\mathrm{m\,s^{-1}}$ and $H = 110\,\mathrm{m}$ yields $\epsilon = 1.15 \times 10^{-6}\,\mathrm{s^{-1}}$, and thus $T_\theta = 9.75 \times 10^5\, H\bar{\zeta}$ according to Eq. B1. This theoretical prediction is in good agreement with the parameterization derived from the velocity data (Eq. 5).

One notes that the buoyancy forcing (e.g. from rivers) does not appear explicitly into Eq. B1. In fact, buoyancy inputs need to interact with a sloping bathymetry to yield a significant transport within a basin [e.g., *Müller*, 2006, chap. 16.2]. If the bathymetry is flat, the pressure gradient simply disappears from the vorticity equation. Thus the main role of the rivers is not to produce a transport but to set the shear within the boundary current (Eq. 3). In absence of winds, the transport is zero and the circulation is limited to an outflow at the surface compensated by an inflow at depth (i.e. the estuarine circulation).

Appendix C: Conservation of Salt

Despite the fact that the model equations are written in terms of freshwater, it can be shown that salinity is also conserved. For the boundary current as a whole, the steady salinity budget is:

$$\begin{aligned} 0 \;=\; & \sum_{i=1}^{2} Q_i^{\mathrm{west}}\, S_i - \sum_{i=1}^{2} Q_i^{\mathrm{east}}\, S_i + \frac{A\,\bar{\zeta}}{\rho_0 f}\,(S_1 - S_2) \\ & + \;\frac{P\,B}{c}\,(S_1 - S_2) \\ & + \;2\,v^*\,(S_2 - S_1) \int_0^{\Theta} (h_1 - H + D)^2\;\frac{R}{L}\,\mathrm{d}\theta. \end{aligned} \tag{C1}$$

where $Q^{\mathrm{west}}, Q^{\mathrm{east}}$ are the volume fluxes forming the boundary current (section 4). Cross-shore Ekman transport and P contribute to the salinity budget by thickening the upper layer at the expense of the lower layer, and the other way around for the eddy fluxes. Note that the ice does not contribute since its mean contribution is zero. The upwelling described in section 4 does not appear either since the model equations are for the water column as a whole (see section Method). Finally, the interior region satisfies an equation similar to Eq. C1 except that $Q^{\mathrm{west}}, Q^{\mathrm{east}}$ are absent, Ekman and eddy fluxes are reversed, and P applies to the area of the interior (A) instead of B.

Acknowledgments. This work is a contribution to the Freshwater–Marine Coupling project of the ArcticNet network of Canada. We thank NSERC and the Canada Research Chairs program for funding. FS acknowledges support from NSF OCE–0927797 and ONR N00014-08-10490. We want to thank the Department of Fisheries and Oceans (DFO) of Canada, their technicians, the captains and crews of the CCGS Radisson, DesGroseillers, Martha Black, and Amundsen. We also thank S. Senneville and J. Caveen for technical support. Data from 1992 were downloaded from DFO's SGDO (Système de Gestion des Données Océanographiques). The associate editor M. Morales-Maqueda and two anonymous reviewers provided helpful comments that improved the manuscript.

References

Barber, D. G., and R. A. Massom (2007), The role of sea ice in Arctic and Antarctic Polynyas, in *Polynyas: Windows to the World*, vol. 74, edited by W. O. Smith and D. G. Barber, pp. 1–54, Elsevier Oceanography Series.

de Verdière, A. C. (2009), Keeping the freedom to build idealized climate models, *Eos*, *90*, 224.

Déry, S. J., M. Stieglitz, E. C. McKenna, and E. F. Wood (2005), Characteristics and trends of river discharge into Hudson, James, and Ungava Bays, 1964–2000, *J. Clim.*, *18*, 2540–2557.

Déry, S. J., M. A. Hernandez-Henriquez, J. E. Burford, and E. F. Wood (2009), Observational evidence of an intensifying hydrological cycle in northern Canada, *Geophys. Res. Lett.*, *36*(L13402), doi:10.1029/2009GL038852.

Déry, S. J., T. J. Mlynowski, M. A. Hernández-Henríquez, and F. Straneo (2011), Interannual variability and and interdecadal trends in Hudson Bay streamflow, *J. Mar. Syst.*, *88*, 341–351, doi:10.1016/j.jmarsys.2010.12.002.

Emery, W. J., and R. E. Thomson (1997), *Data analysis methods in physical oceanography*, 2 ed., 638 pp., Elsevier.

Galbraith, P. S., and P. Larouche (2011), Sea-surface temperature in Hudson Bay and Hudson Strait in relation to air temperature and ice cover breakup, 1985–2009, *J. Mar. Syst.*, *87*, 66–78, doi:10.1016/j.jmarsys.2011.03.002.

Gill, A. (1982), *Atmosphere-ocean dynamics.*, Academic Press, London (UK).

Gosselin, M., L. Legendre, J.-C. Therriault, and S. Demers (1990), Light and nutrient limitations of sea-ice microalgae (Hudson Bay, Canadian Arctic), *J. Phycol.*, *26*, 220–232.

Granskog, M. A., Z. A. Kuzyk, K. Azetsu-Scott, , and R. W. Macdonald (2011), Distributions of runoff, sea-ice melt and brine using δ^{18}O and salinity data—a new view on freshwater cycling in Hudson Bay, *J. Mar. Syst.*, *88*, 362–374, doi:10.1016/j.jmarsys.2011.03.011.

Hochheim, K. P., and D. Barber (2010), Atmospheric forcing of sea ice in Hudson Bay during the fall period, 1980–2005, *J. Geophys. Res.*, *115*(C05009), doi:10.1029/2009JC005334.

Hochheim, K. P., J. K. Lukovich, and D. G. Barber (2011), Atmospheric forcing of sea ice in Hudson Bay during the spring period, 1980–2005, *J. Mar. Syst.*, *88*, 476–487, doi:10.1016/j.jmarsys.2011.05.003.

Hunke, E. C., and J. K. Dukowicz (1997), An elastic-viscous-plastic model for sea ice dynamics, *J. Phys. Oceanogr.*, *27*, 1849–1867.

Ingram, R., and S. Prinsenberg (1998), Coastal oceanography of Hudson Bay and surrounding eastern Canadian Arctic waters, in *The Sea*, vol. 11, edited by A. Robinson and K. Brink, pp. 835–861, Chichester UK Wiley.

Lammers, R. B., A. I. Shiklomanov, C. J. Vörösmarty, B. M. Fekete, and B. J. Peterson (2001), Assessment of contemporary Arctic river runoff based on observational discharge records, *J. Geophys. Res.*, *106*, 3321–3334.

Lapoussière, A., C. Michel, M. Gosselin, and M. Poulin (2009), Spatial variability in organic material sinking export in the Hudson Bay system, Canada, during fall, *Cont. Shelf Res.*, *29*, 1276–1288, doi:10.1016/j.csr.2009.02.004.

Markham, W. (1986), The ice cover, in *Canadian Inland Seas*, edited by I. Martini, pp. 101–116, Elsevier oceanogr. series.

Maxwell, J. B. (1986), A climate overview of the Canadian inland seas, in *Canadian Inland Seas*, edited by I. Martini, pp. 79–99, Elsevier oceanogr. series.

Mesinger, F., et al. (2006), North American Regional Reanalysis: A long-term, consistent, high-resolution climate dataset for the North American domain, as a major improvement upon the earlier global reanalysis datasets in both resolution and accuracy, *Bull. Amer. Meteor. Soc.*, *87*, 343–360.

Müller, P. (2006), *The Equations of Oceanic Motions*, 1st ed., Cambridge University Press.

Murty, T. S., and F. G. Barber (1974), An assessment of ice transport in the Hudson Bay region, in *Proceedings of the Second International Conference on Port and Ocean Engineering under Arctic Conditions*, pp. 441–450, University of Iceland.

Newton, R., B. Tremblay, M. A. Cane, and P. Schlosser (2006), A simple model of the Arctic Ocean response to annular atmospheric modes, *J. Geophys. Res.*, *111*(C09019), doi:10.1029/2004JC002622.

NOAA (2006), 2-minute gridded global relief data (Etopo2v2), *Tech. rep.*, U.S. Department of Commerce, National Geophysical Data Center.

Nof, D. (2008), Simple versus complex climate modeling, *Eos*, *89*, 544–545.

NSIDC (2011), What is the Arctic?, Retrieved from http://nsidc.org/arcticmet/basics/arctic_definition.html, Education Center on Arctic Climatology and Meteorology, National Snow and Ice Data Center.

Pedlosky, J. (1987), *Geophysical Fluid Dynamics*, 2 ed., 710 pp., Springer.

Prinsenberg, S. J. (1984), Freshwater contents and heat budgets of James Bay and Hudson Bay, *Cont. Shelf Res.*, *3*, 191–200.

Prinsenberg, S. J. (1986a), Salinity and temperature distributions of Hudson Bay and James Bay, in *Canadian Inland Seas*, edited by I. Martini, pp. 163–186, Elsevier oceanogr. series.

Prinsenberg, S. J. (1986b), The circulation pattern and current structure of Hudson Bay, in *Canadian Inland Seas*, edited by I. Martini, pp. 187–203, Elsevier oceanogr. series.

Prinsenberg, S. J. (1988), Ice-cover and ice-ridge contributions to the freshwater contents of Hudson Bay and Foxe Basin., *Arctic*, *41*, 6–11.

Saucier, F. J., S. Senneville, S. J. Prinsenberg, F. Roy, G. Smith, P. Gachon, D. Caya, and R. Laprise (2004), Modelling the sea ice-ocean seasonal cycle in Hudson Bay, Foxe Basin and Hudson Strait, Canada, *Clim. Dyn.*, *23*, 303–326, doi:10.1007/s00382-004-0445-6.

Spall, M. A. (2004), Boundary currents and watermass transformation in marginal seas, *J. Phys. Oceanogr.*, *34*, 1197–1213.

St-Laurent, P., F. Straneo, J.-F. Dumais, and D. G. Barber (2011), What is the fate of the river waters of Hudson Bay?, *J. Mar. Syst.*, *88*, 352–361, doi:10.1016/j.jmarsys.2011.02.004.

Stouffer, R. J., et al. (2006), Investigating the causes of the response of the thermohaline circulation to past and future climate changes, *J. Clim.*, *19*, 1365–1387.

Straneo, F. (2006), On the connection between dense water formation, overturning, and poleward heat transport in a convective basin, *J. Phys. Oceanogr.*, *36*, 1822–1840.

Straneo, F., and F. J. Saucier (2008a), The outflow from Hudson Strait and its contribution to the Labrador Current, *Deep Sea-Res. I*, *55*, 926–946, doi:10.1016/j.dsr.2008.03.012.

Straneo, F., and F. J. Saucier (2008b), The Arctic-subarctic exchange through Hudson Strait, in *Arctic-Subarctic ocean fluxes*, edited by R. Dickson, J. Meincke, and P. Rhines, pp. 249–261, Springer Science.

Tan, F. C., and P. M. Strain (1996), Sea ice and oxygen isotopes in Foxe Basin, Hudson Bay, and Hudson Strait, Canada, *J. Geophys. Res.*, *101*(C9), 20,869–20,876.

Tucker, W. B., A. J. Gow, and J. A. Richter (1984), On small-scale horizontal variations of salinity in first-year sea ice, *J. Geophys. Res.*, *89*(C4), 6505–6514.

Wåhlin, A. K., and H. L. Johnson (2009), The salinity, heat, and buoyancy budgets of a coastal current in a marginal sea, *J. Phys. Oceanogr.*, *39*, 2562–2580, doi:10.1175/2009JPO4090.1.

Wan, H., X. L. Wang, and V. R. Swail (2010), Homogenization and trend analysis of Canadian near-surface wind speeds, *J. Clim.*, *23*, 1209–1225, doi:10.1175/2009jcli3200.1.

Wang, J., L. Mysak, and R. G. Ingram (1994), A three-dimensional numerical simulation of Hudson Bay summer ocean circulation: Topographic gyres, separations, and coastal jets, *J. Phys. Oceanogr.*, *24*, 2496–2514.

D.G. Barber, Centre for Earth Observation Science, University of Manitoba, Wallace Building, 125 Dysart Rd, Winnipeg, MA R3T 2N2, Canada.

P. St-Laurent, Center for Coastal Physical Oceanography, Old Dominion University, 4111 Monarch Way, Norfolk, VA 23508, USA. (pierre@ccpo.odu.edu)

F. Straneo, Department of Physical Oceanography, Woods Hole Oceanographic Institution, MS 21, Woods Hole, MA 02543, USA.

Table 1. Variables calculated by the model, model parameters, and forcings. See Method and Fig. 3 for further description of the symbols.

Variable	Meaning	Calculation
$D\,(t)$	Thick. layer 2 interior	Eq. 7.
$h_1\,(\theta, t)$	Thick. layer 1 boundary	Eq. 8.
$h_2\,(\theta, t)$	Thick. layer 2 boundary	$h_2 = H - h_1$
$V_1\,(\theta, t)$	Vel. layer 1 boundary	Eqs. 3,4.
$V_2\,(\theta, t)$	Vel. layer 2 boundary	Eqs. 3,4.
ρ_1 ($1023.8\,\mathrm{kg\,m^{-3}}$ in Run #1)	Density layer 1	Eqs. 7,8 with $\partial/\partial t \to 0$.
Parameter	**Value**	**Source**
Coriolis parameter, f	$1.2 \times 10^{-4}\,\mathrm{rad\,s^{-1}}$	*NOAA* [2006]
Arc covered by basin, Θ	293°	*NOAA* [2006]
Bottom depth, H	110 m	*NOAA* [2006]
Radius basin, $R + L$	673 km	*NOAA* [2006]
Width boundary region, L	70 km	*St-Laurent et al.* [2011, Fig. 4]
Area interior region, A	$4.22 \times 10^5\,\mathrm{km^2}$	*St-Laurent et al.* [2011, Fig. 4]
Area boundary, B	$2.55 \times 10^5\,\mathrm{km^2}$	$\int_0^\Theta \int_R^{R+L} r\,\mathrm{d}r\,\mathrm{d}\theta$
Salinity of sea ice, S_{ice}	5 psu	*Tucker et al.* [1984]
Density reference, ρ_0	$1000\,\mathrm{kg\,m^{-3}}$	—
Density of sea ice, ρ_{ice}	$900\ \mathrm{kg\,m^{-3}}$	*Hunke and Dukowicz* [1997]
Density bottom layer, ρ_2	$1026.5\,\mathrm{kg\,m^{-3}}$	*St-Laurent et al.* [2011, Fig. 2]
Haline contraction, β	0.8×10^{-3}	—
Eddy flux efficiency, v^*	$1\,\mathrm{m\,s^{-1}}$	Visual fit to observations.
Transport-wind relation, a	$10^6\,\mathrm{m^2\,Pa^{-1}\,s^{-1}}$	Table 2
Forcing	**Value**	**Source**
Precip. minus Evap., P	$1\,\mathrm{mm\,day^{-1}}$	*St-Laurent et al.* [2011, Table 1]
Sea ice thickness	0–1.47 m	*St-Laurent et al.* [2011, Table 1]
FW inflow, $\mathrm{FWI} = h_1 V_1 L\,c$	$2500\,\mathrm{m^3\,s^{-1}}$	*St-Laurent et al.* [2011, Table 1]
River runoff, T_{riv}	Varies time & space	*Saucier et al.* [2004], *Déry et al.* [2009]
Wind stress curl, $\overline{\zeta}$	Varies in time	*Mesinger et al.* [2006]

Table 2. Correlation and regression between observed velocity and the wind stress curl used as model forcing. The correlation is R, p the significance, N the effective number of degrees of freedom [*Emery and Thomson*, 1997, chap. 3.15], and the linear regression is $v = a\overline{\zeta} + v_0$.

Station	Depth	R	p	N	a	v_0	Period
	m				$\mathrm{m^2\,Pa^{-1}\,s^{-1}}$	$\mathrm{cm\,s^{-1}}$	
A	10	0.35	0.18	16	5.4×10^5	1.4	Aug. 2003–Jul. 2004
A	70	0.63	< 0.01	18	3.7×10^5	1.8	Aug. 2003–Jul. 2004
B	28	0.69	< 0.01	19	2.9×10^6	0.3	Sept. 1992–Aug. 1993
B	58	0.70	< 0.01	19	2.5×10^6	-5.1	Sept. 1992–Aug. 1993
B	123	0.72	0.01	11	2.0×10^6	-7.3	Sept. 1992–Aug. 1993

Table 3. Comparison between observations (Obs.) and simulation (Sim.). The table provides the first two moments (mean ± standard deviation) for the curves of Figs. 11,12,13,14.

Fig.	11	11	12	12	13	14
	V_1	V_2	V_1	V_2	S	FWE
	$\mathrm{cm\,s^{-1}}$	$\mathrm{cm\,s^{-1}}$	$\mathrm{cm\,s^{-1}}$	$\mathrm{cm\,s^{-1}}$	psu	mSv
Obs.	5.9 ± 8.1	-3.6 ± 4.6	2.3 ± 2.7	2.7 ± 1.6	29.8 ± 0.8	28.0 ± 20
Sim.	10.5 ± 2.5	-3.3 ± 1.5	2.3 ± 0.7	1.9 ± 3.1	29.9 ± 0.7	32.7 ± 14

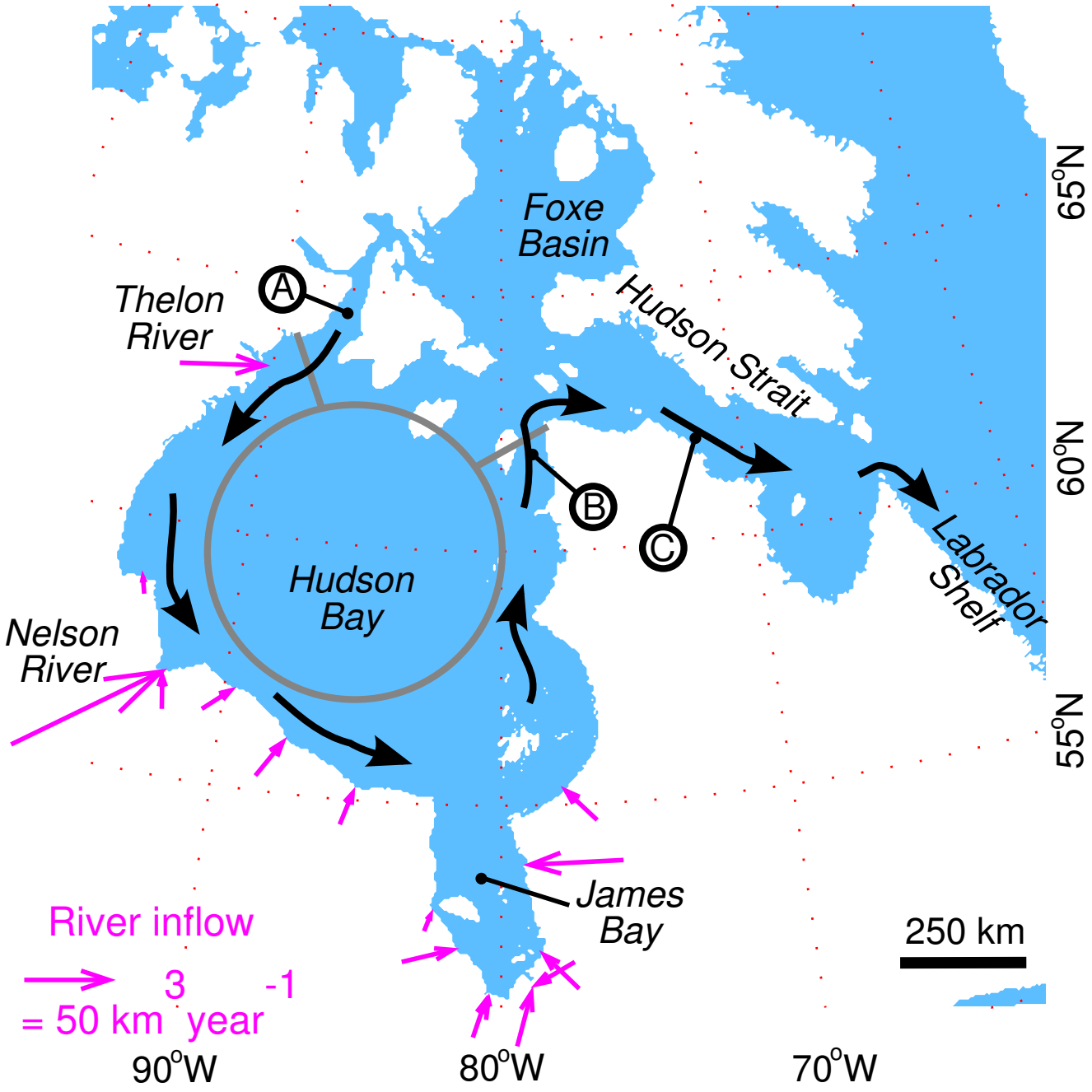

Figure 1. Map of Hudson Bay and the surrounding basins. The black arrows represent the mean surface circulation according to *Prinsenberg* [1986b] and *St-Laurent et al.* [2011]. The magenta arrows indicate the location of river discharge and its mean value. The approximate divisions of the conceptual model are given by the gray lines. Circled letters show the location of the instruments used in the study.

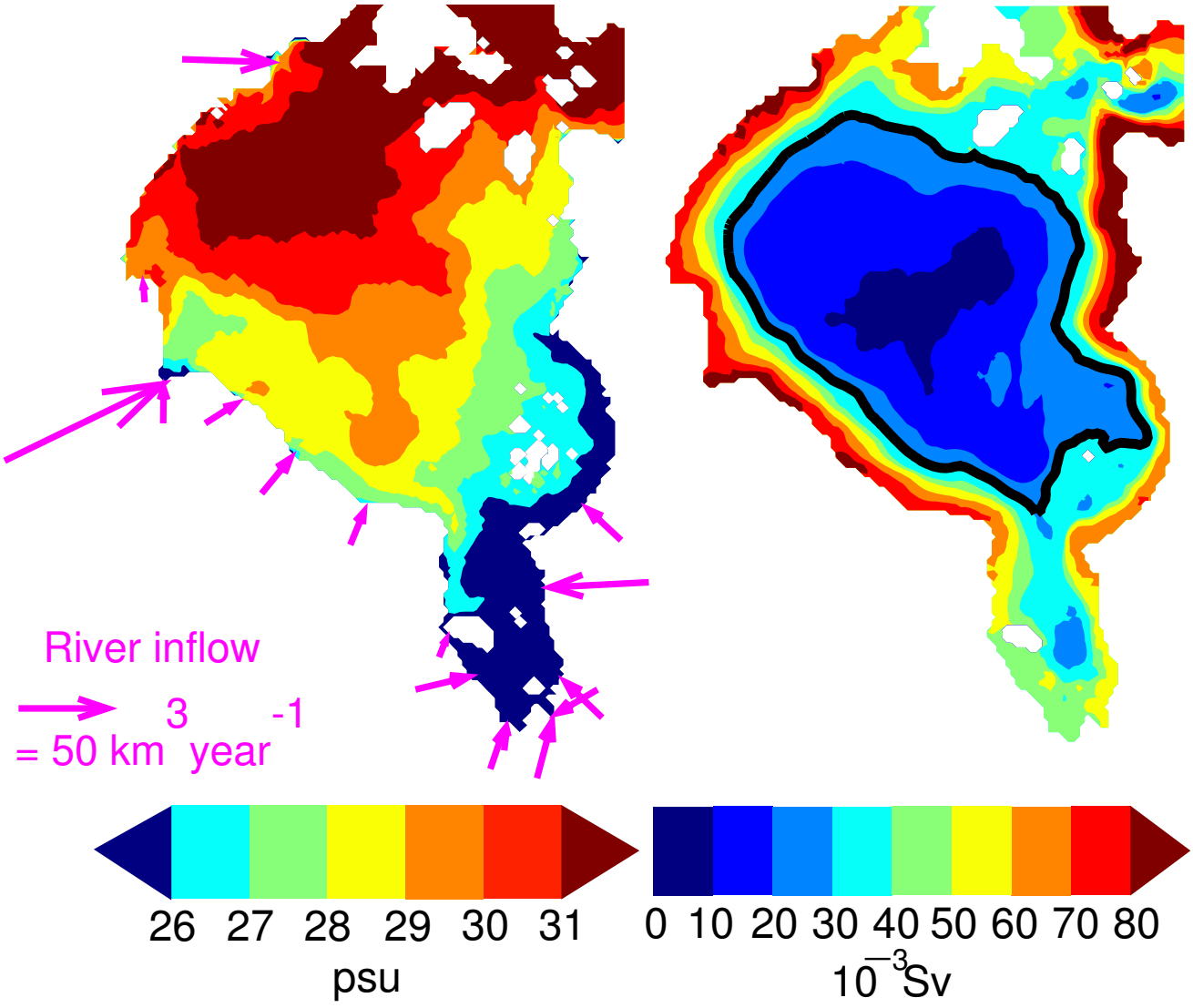

Figure 2. Results from realistic simulations with a 3–D sea ice-ocean coupled model. (left) Sea surface salinity during the summer season. The arrows give the location and magnitude of river inflow. (right) Streamfunction for the surface circulation. The panel is taken from *St-Laurent et al.* [2011].

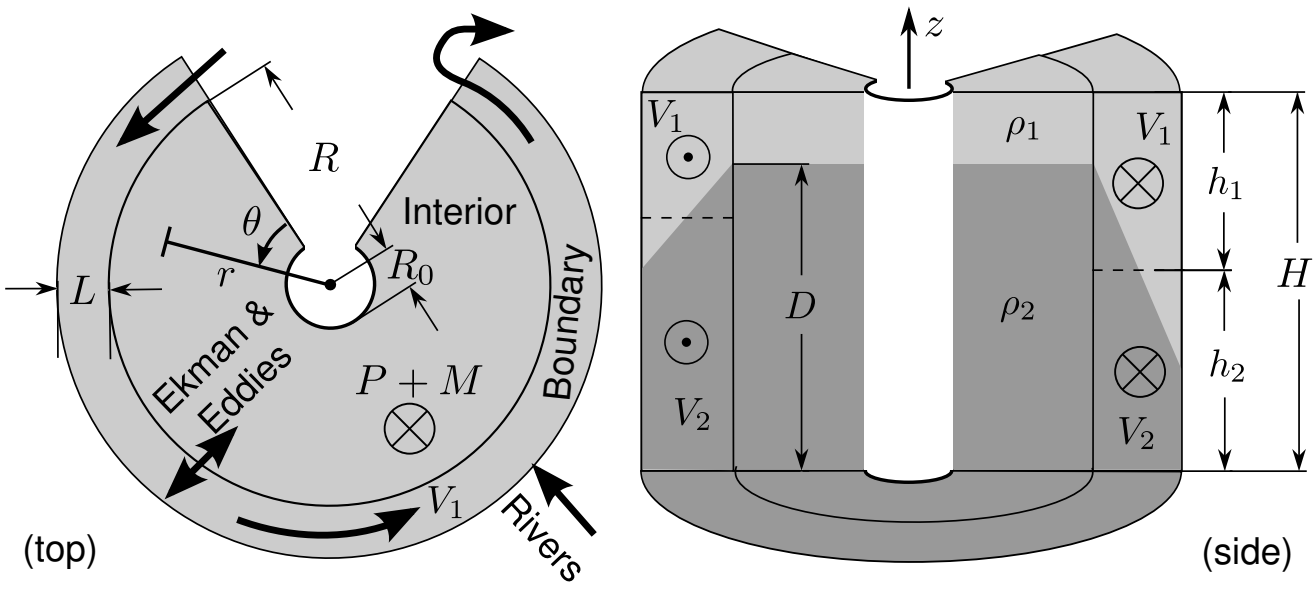

Figure 3. Top and side views of the conceptual model. The geometry is cylindrical with coordinates (r, θ, z) and corresponding velocities (u, v, w). See Table 1 and Method for a definition of the symbols.

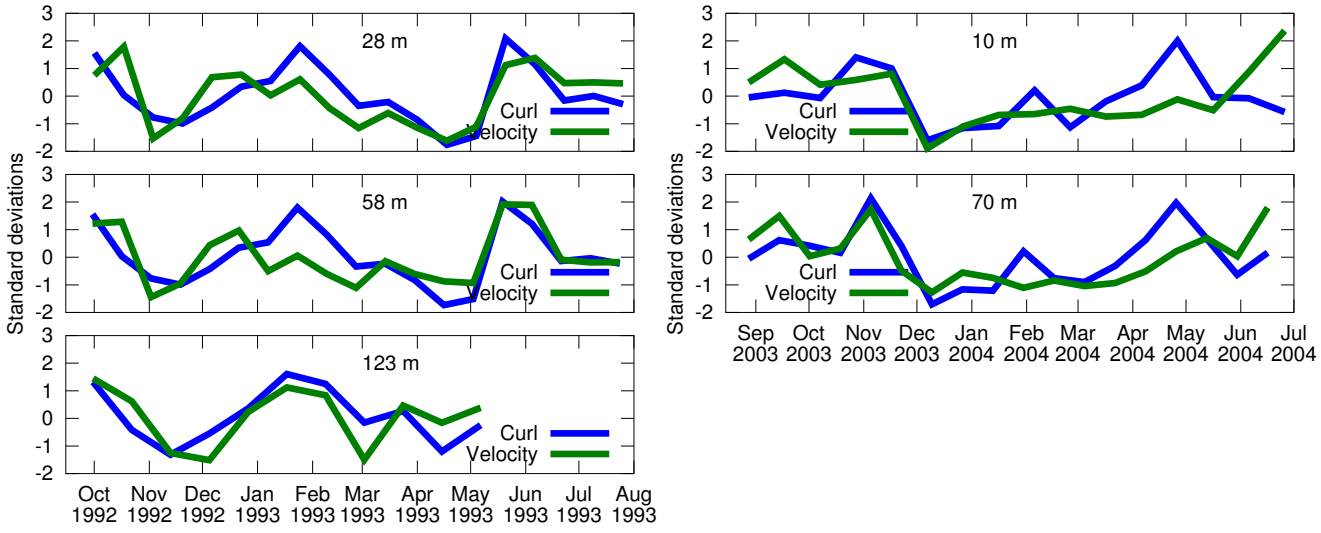

Figure 4. Comparison between observed velocities (left: Station B; right: Station A; see Fig. 1) and the wind stress curl used as model forcing (see Method). The curl timeseries may differ slightly from one panel to another according to the effective number of degrees of freedom (see Table 2).

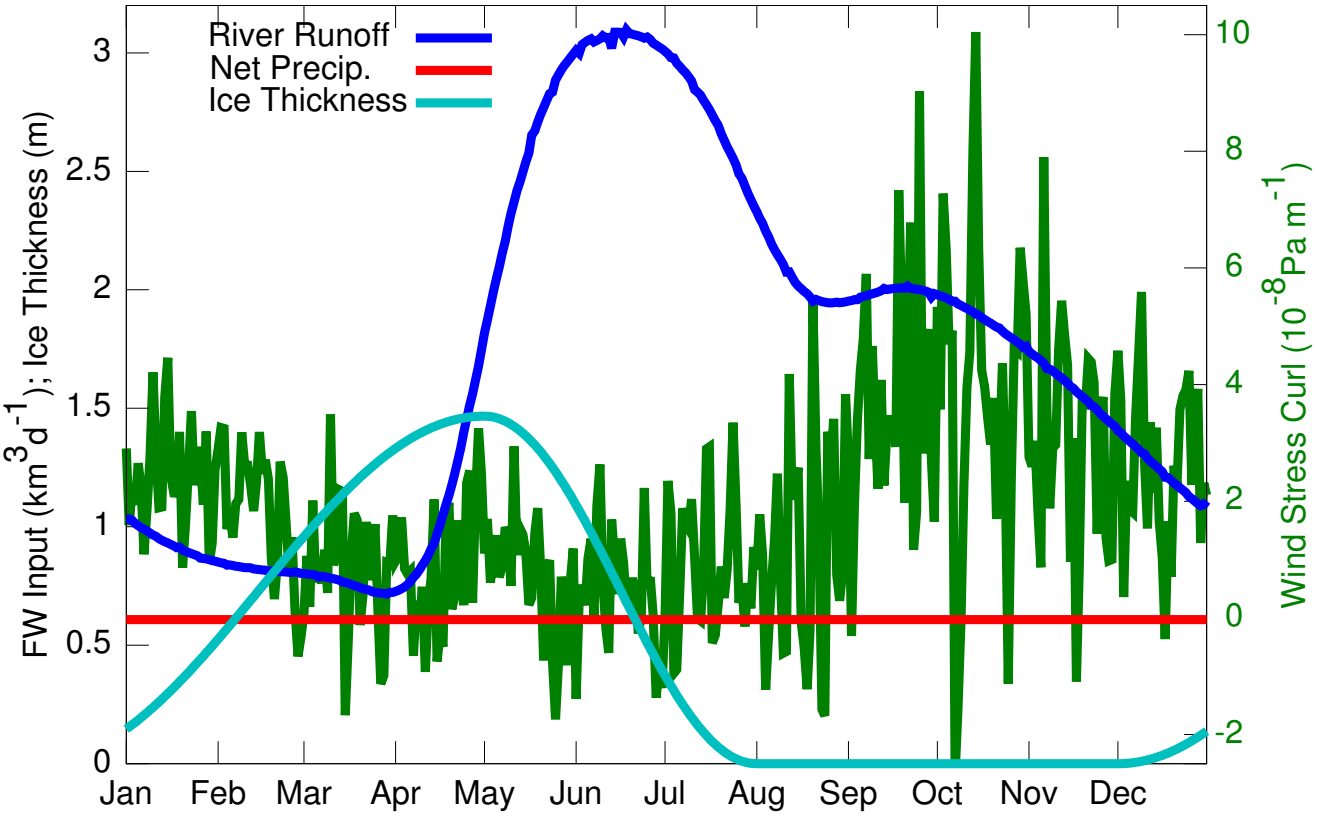

Figure 5. Climatological seasonality of the hydrological, cryospheric, and atmospheric components of Hudson and James bays, obtained by averaging the model forcings over the period 1979–2007 (see Method). Note the strong cyclonic winds during the fall season.

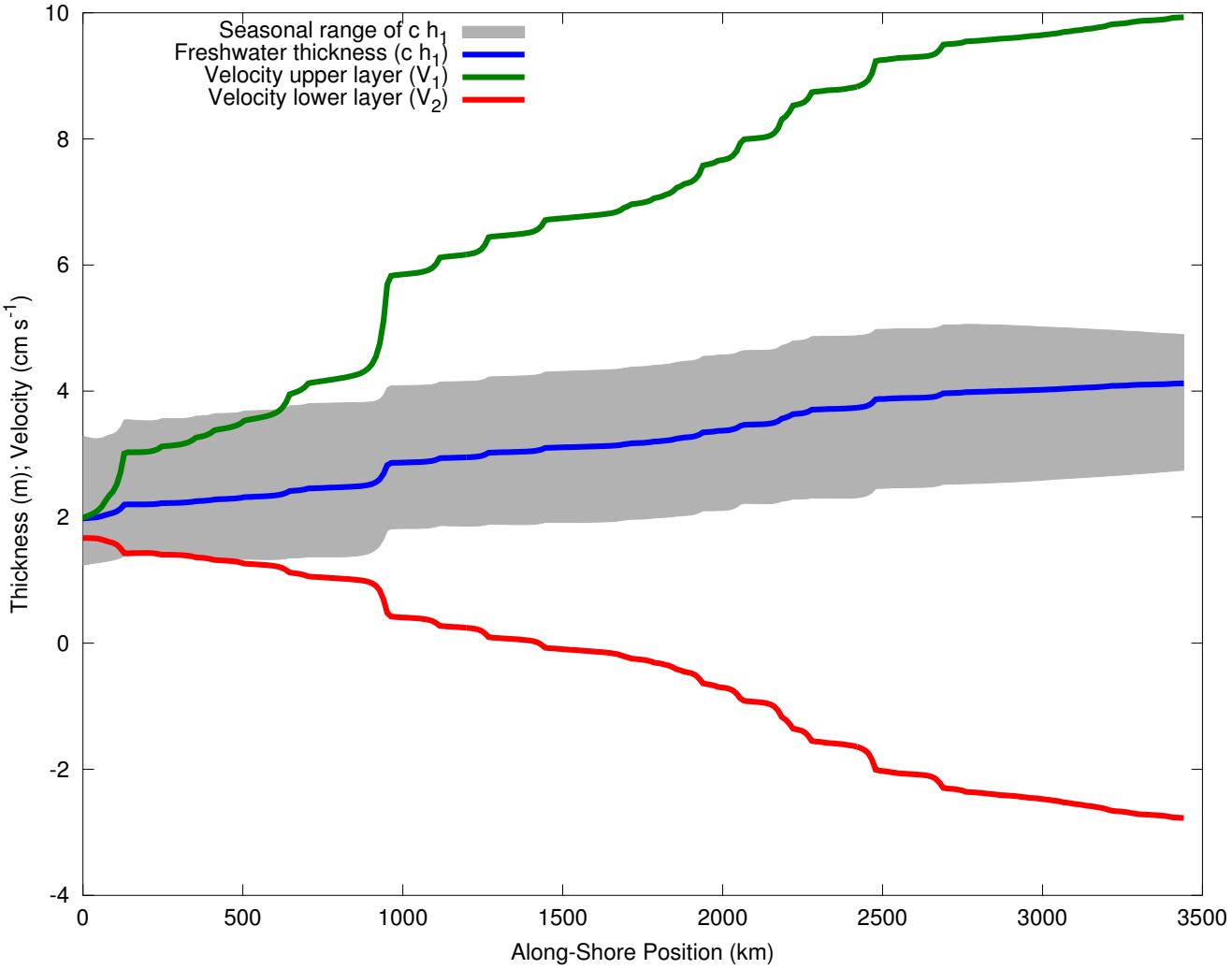

Figure 6. Freshwater thickness ($c\,h_1$) and velocities (V_1, V_2) in the boundary current, averaged over the full period (1979–2007) of the control simulation (Run #1; see section 3.5). The grey area is the seasonal range for the freshwater thickness. The along-shore position increases in a counter-clockwise sense, starting from the upstream boundary of the model (northwestern Hudson Bay).

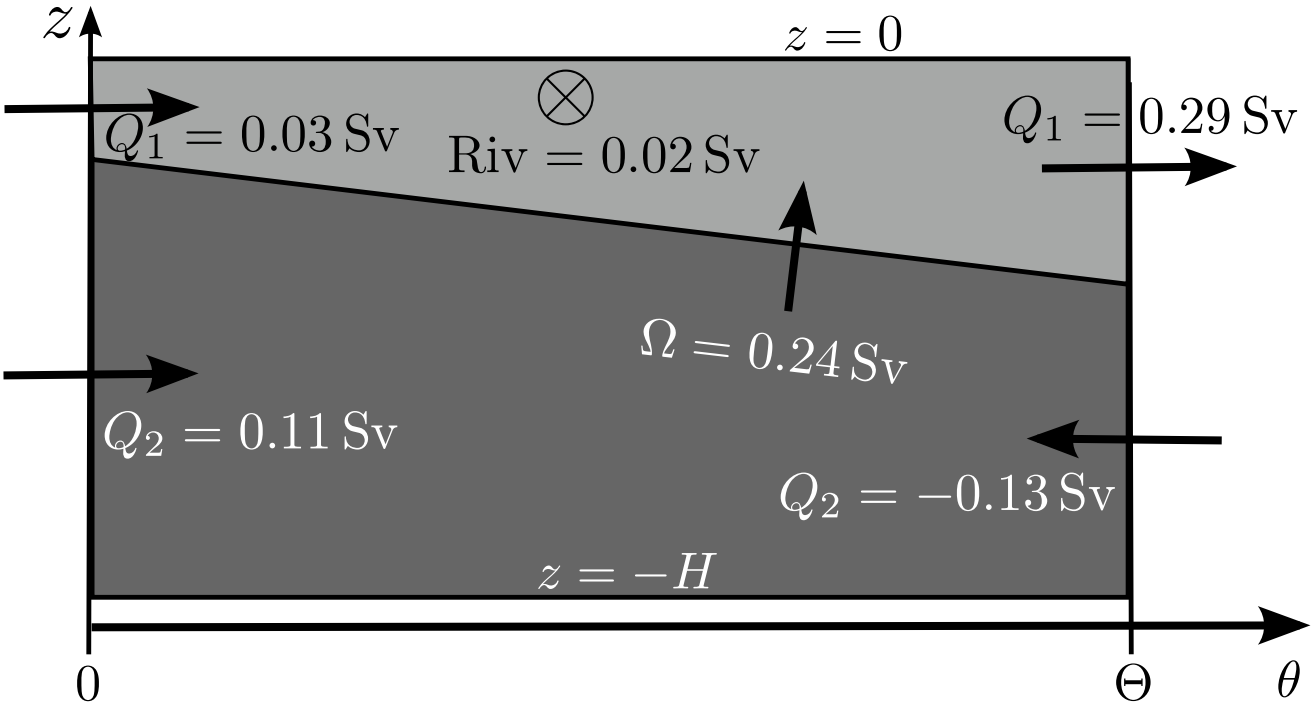

Figure 7. Mean volume budget for the boundary region of the model (Run #1). The light (dark) gray color represents the upper (lower) layer having subscript 1 (2). Q_i is the velocity of layer i integrated laterally (from $r = R$ to $r = R + L$) and vertically (over the layer thickness). $\theta = 0$ and $\theta = \Theta$ refer to the northwestern and northeastern limits of the boundary region, respectively.

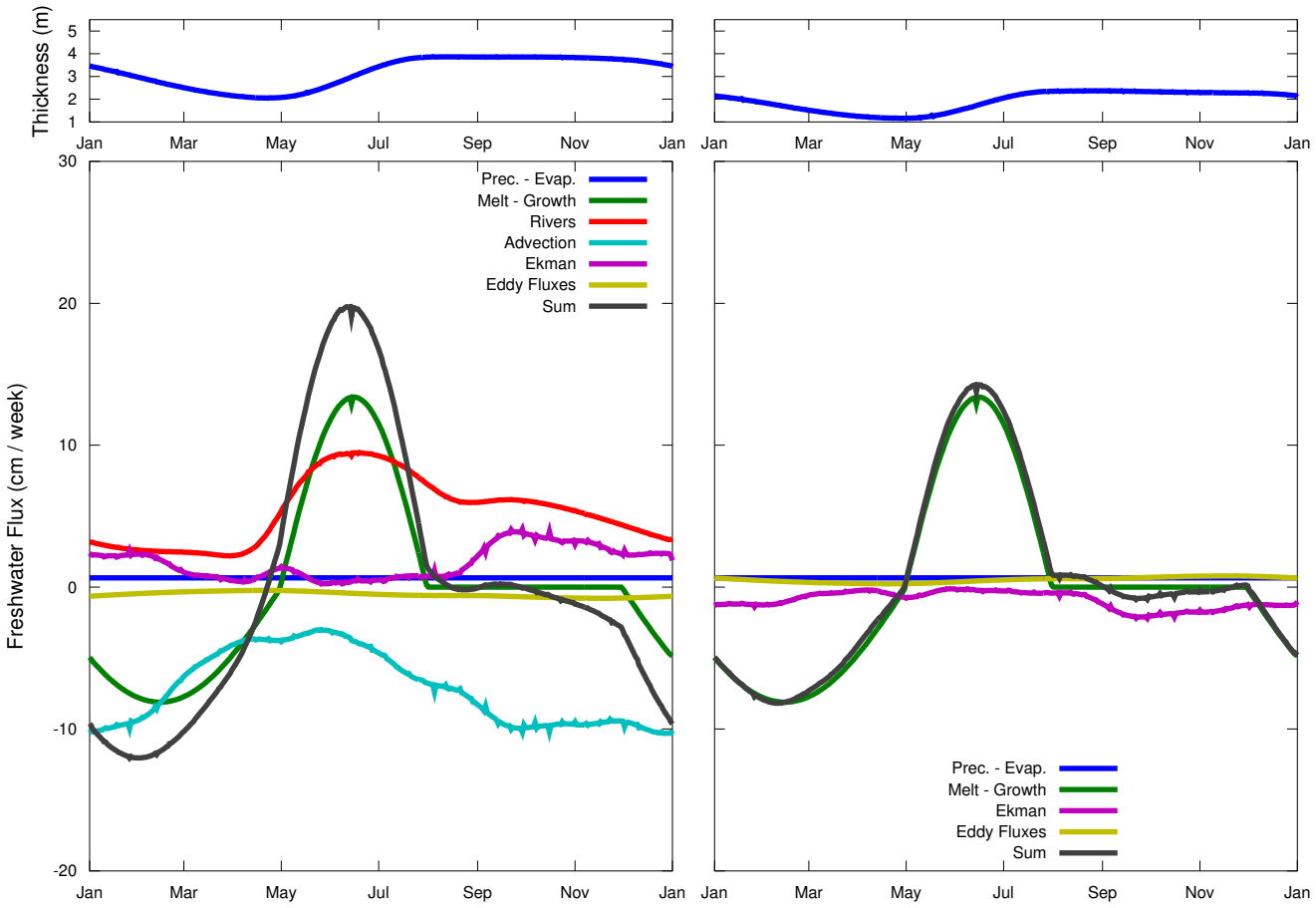

Figure 8. Mean seasonal freshwater budget (1979–2007) for the (left) boundary and (right) interior regions of Hudson Bay (Run #1). The different curves give the magnitude of each term in Eqs. 8 (left panel) and 7 (right panel), averaged over the area of the boundary region (left panel) and interior region (right panel). The sum of the terms (gray curve) gives the seasonal gain/loss of freshwater. The upper panel shows the average thickness of freshwater over the year. The vertical scale of the figure is the same as in Fig. 10 to ease the comparison.

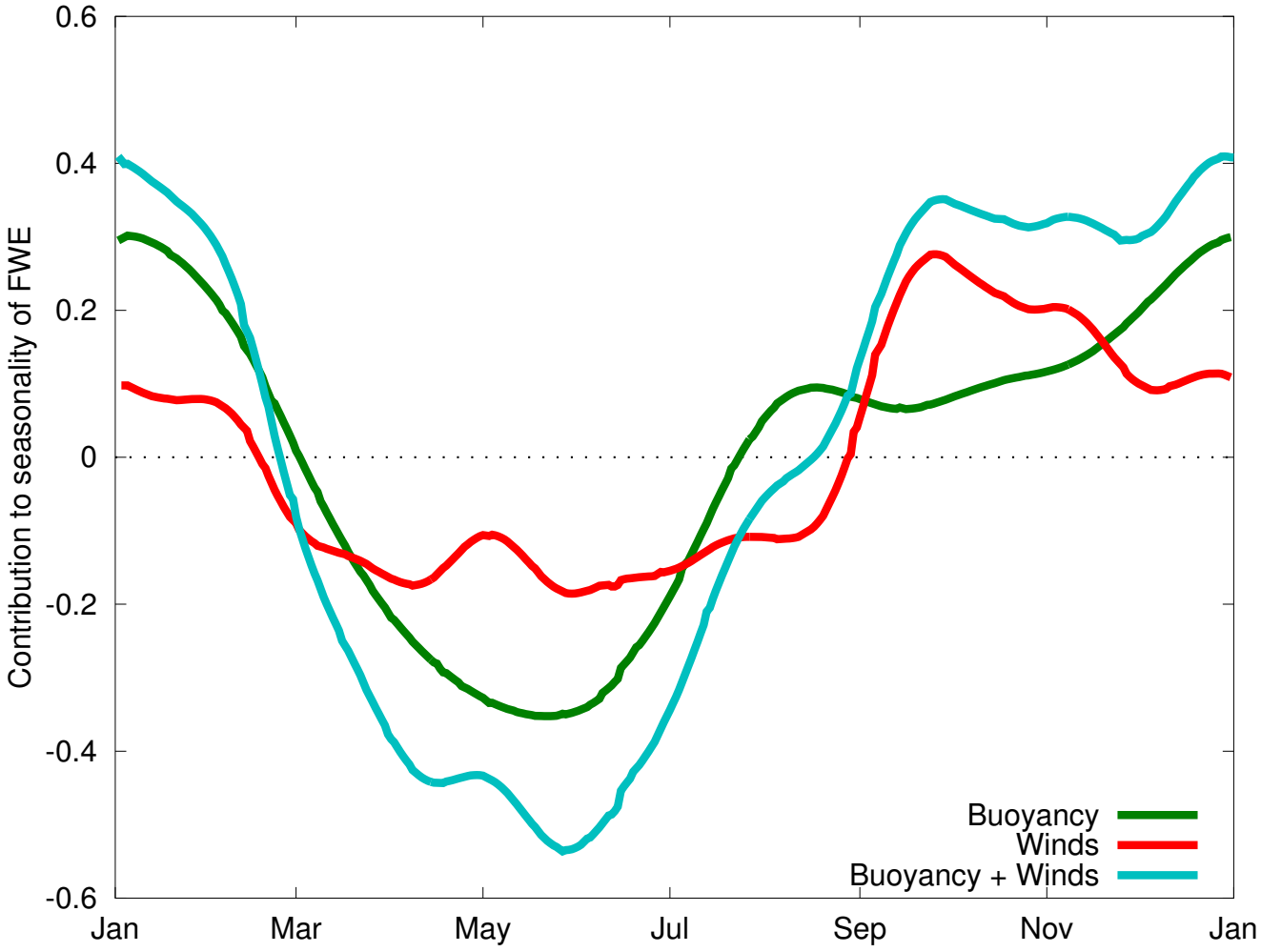

Figure 9. Relative contribution of buoyancy inputs, $CB'/\langle CW + CB\rangle$, and winds, $CW'/\langle CW + CB\rangle$, to the seasonal FreshWater Export (FWE). See Eqs. 15,16 for the definition of the terms. The seasonal variability corresponds to an average of the years 1979–2007.

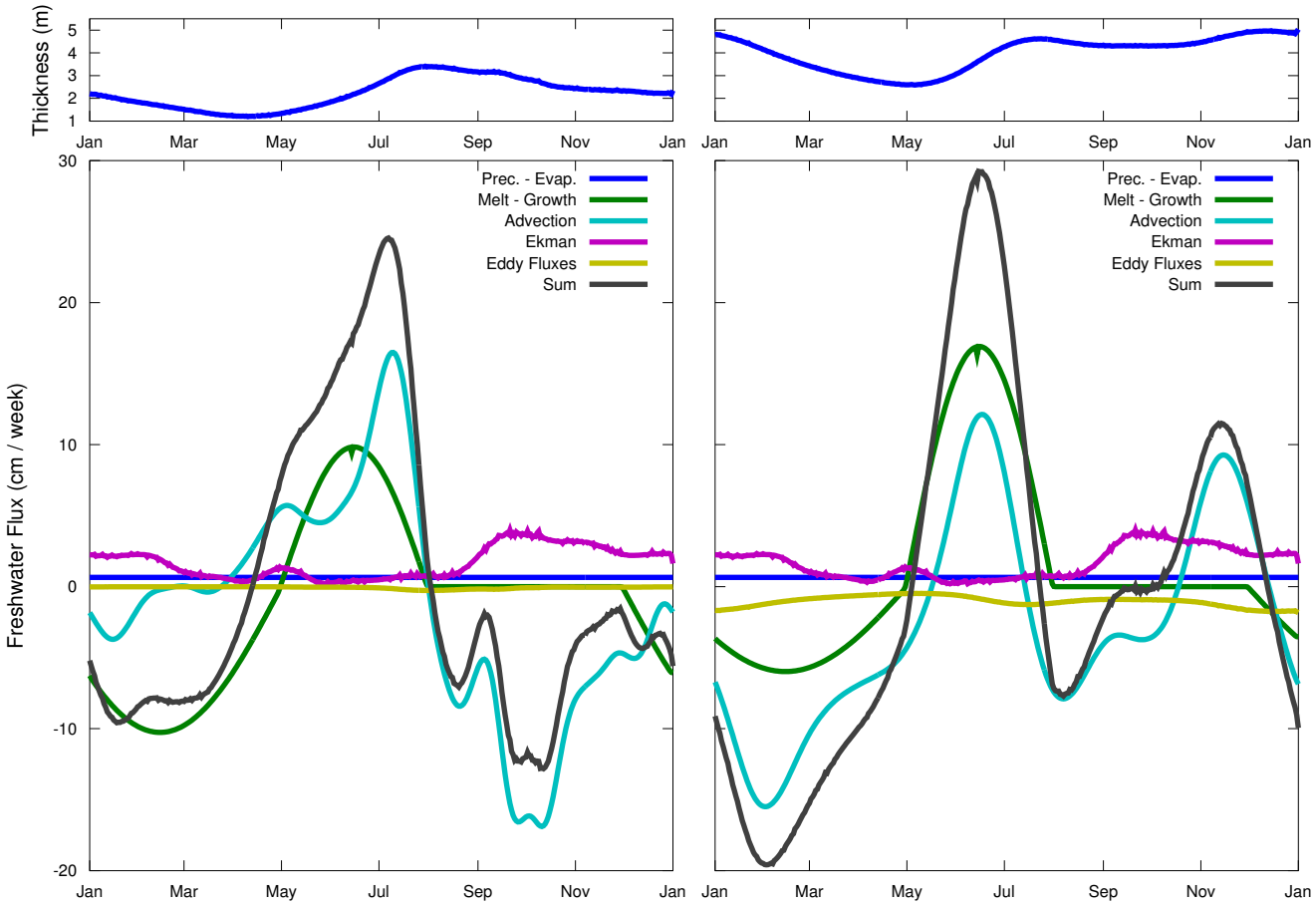

Figure 10. Same as in Fig. 8 but at two points of the boundary current representative of (left) western HJB, $\theta = 0.16\,\Theta$, and (right) eastern HJB, $\theta = 0.84\,\Theta$ (Run #2).

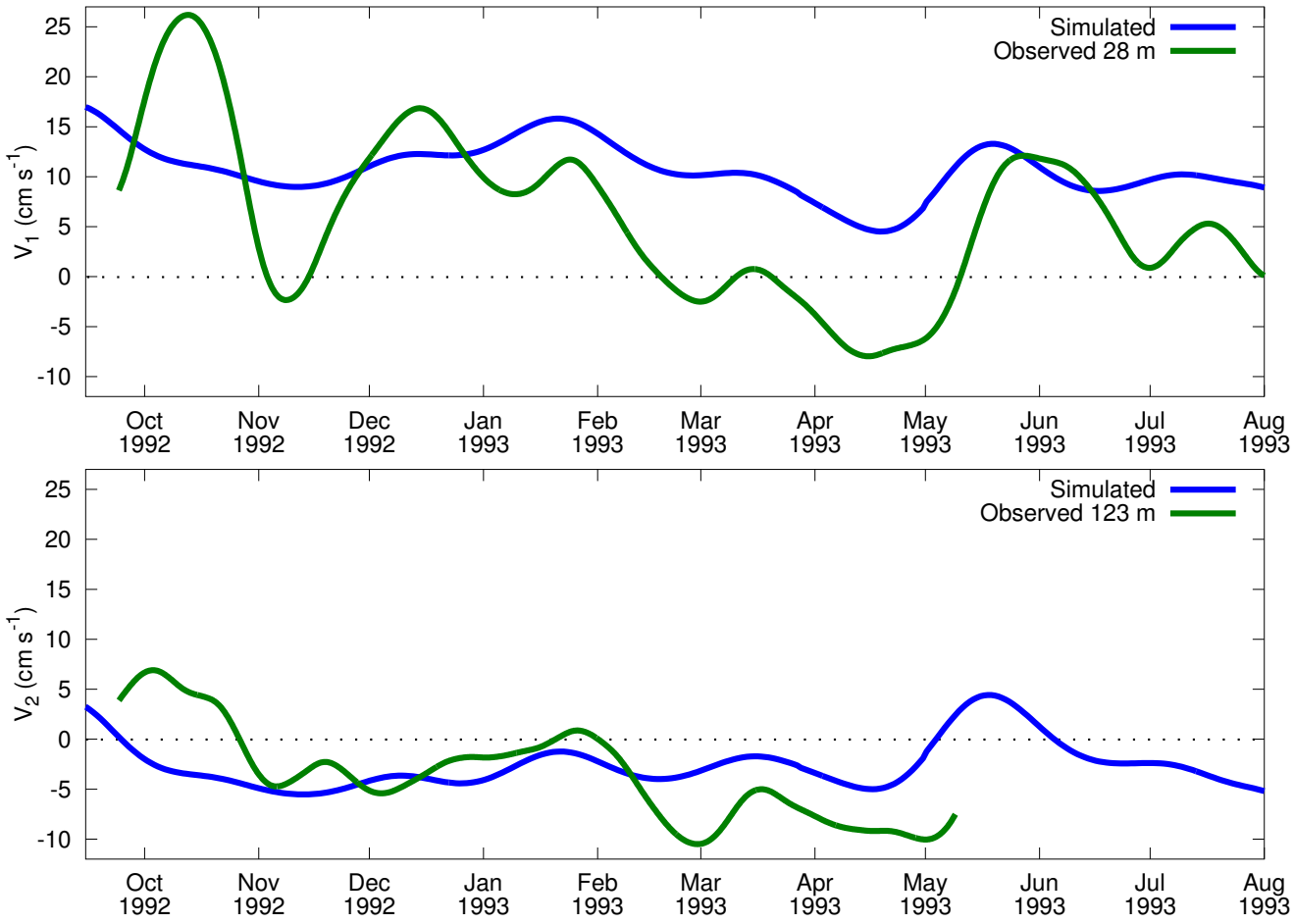

Figure 11. Comparison between observed and simulated (Run #1) velocities at station B (northeastern Hudson Bay; see Fig. 1). V_1 (V_2) is the velocity in the upper (lower) model layer. Data from the lower current-meter are not available after May 1993. Note the episodes of flow reversal in V_2.

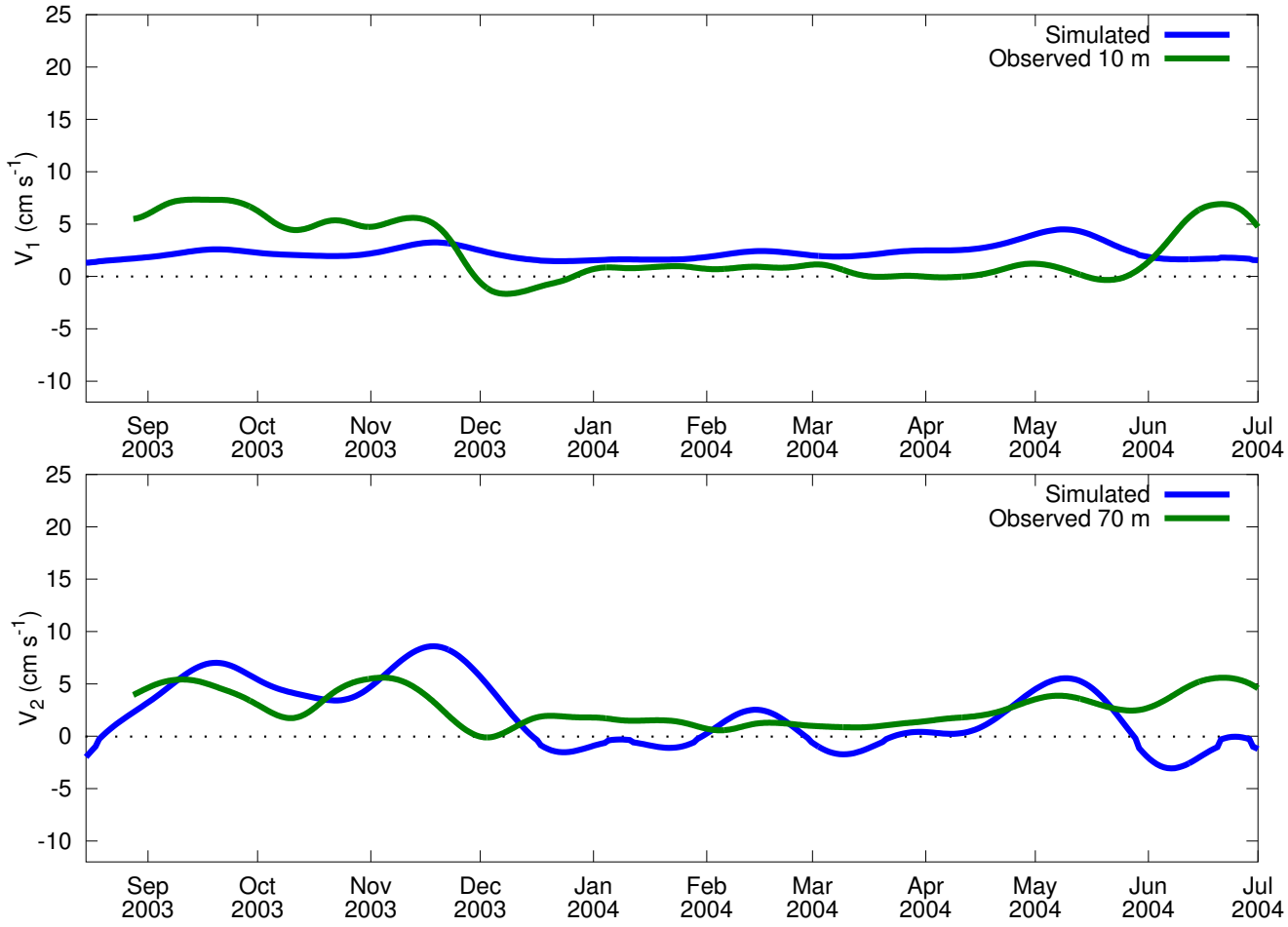

Figure 12. Comparison between observed and simulated (Run #1) velocities at Station A (northwestern Hudson Bay; see Fig. 1). V_1 (V_2) is the velocity in the upper (lower) model layer. The vertical scale is the same as in Fig. 11 to ease the comparison.

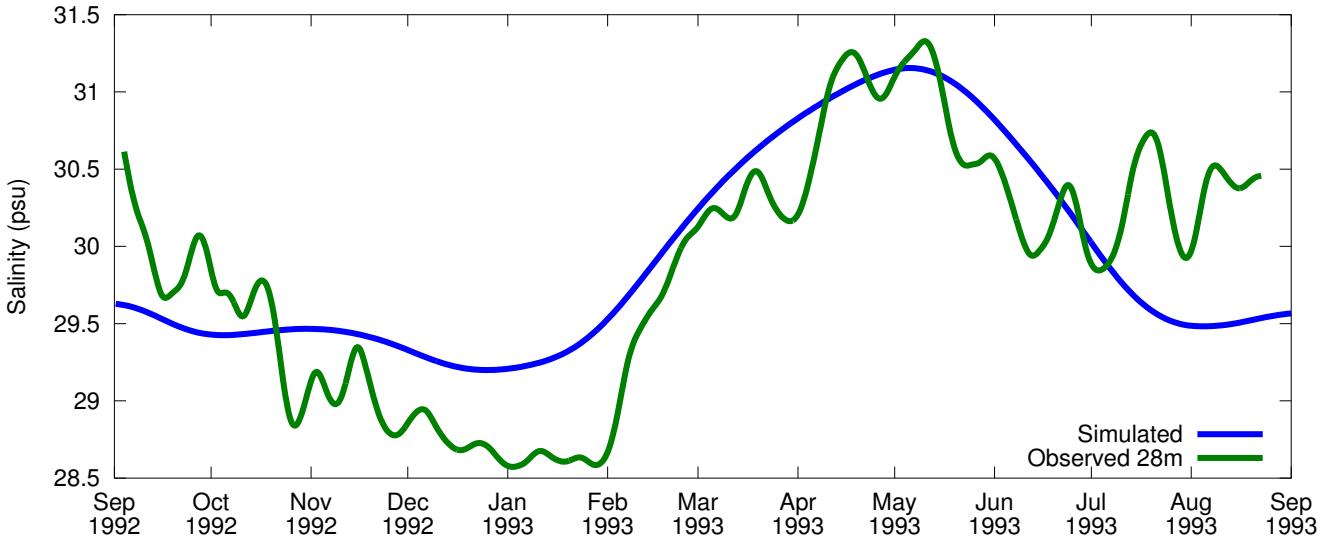

Figure 13. Comparison between observed salinity at station B and the pseudo-salinity derived from the control simulation (Run #1) by assuming a fixed pycnocline depth.

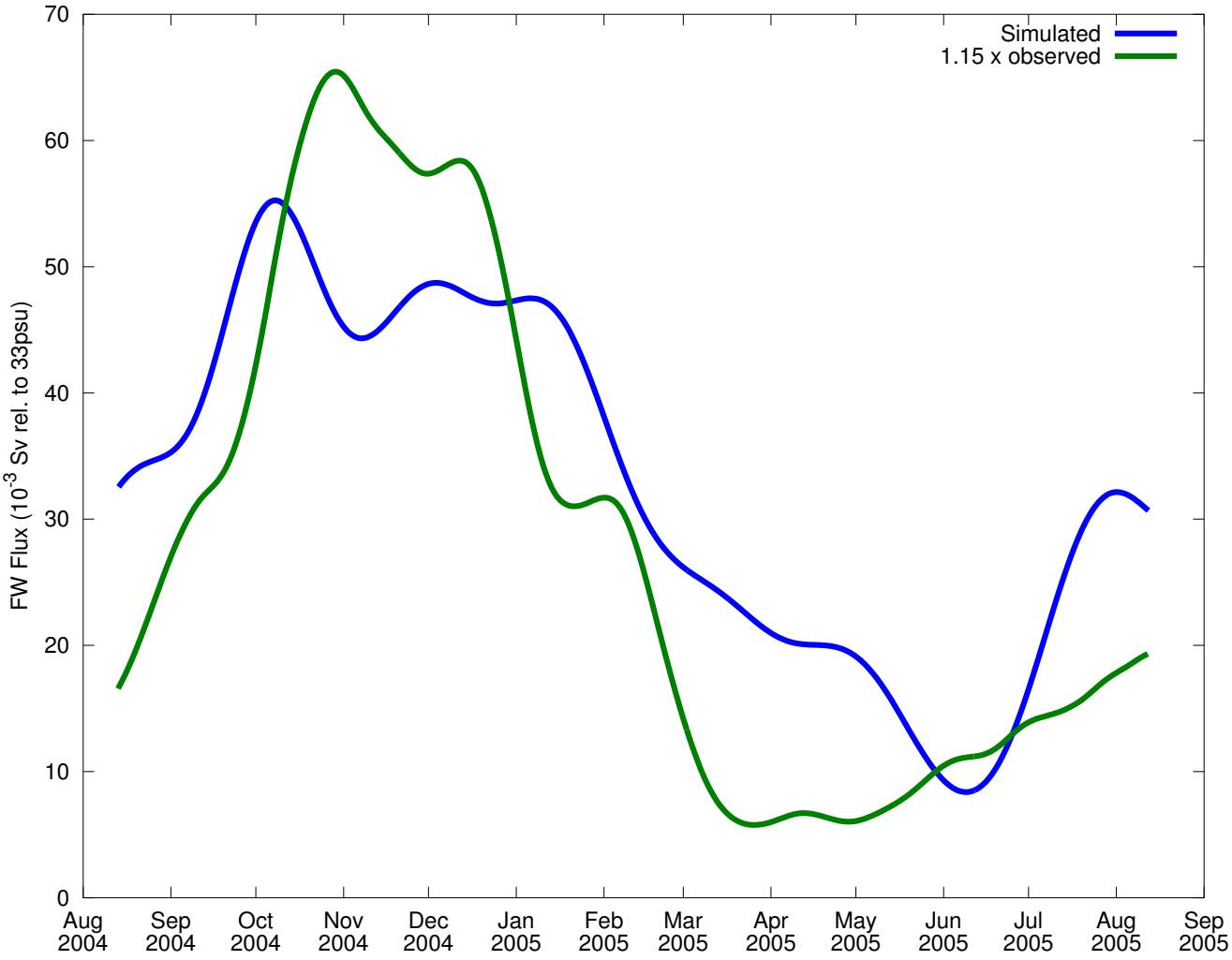

Figure 14. Comparison between observed and simulated freshwater flux downstream of Hudson Bay. Observations [*Straneo and Saucier*, 2008a] are from Station C and model results from Station B (see Fig. 1; model results are from Run #1). The instruments did not cover the full width of the current and the authors estimate the true value to be 1.15 times the observed flux.